From molecular oxo-hydroxo Ce clusters to crystalline CeO2

Estevenon, P.; Amidani, L.; Bauters, S.; Tamain, C.; Bodensteiner, M.; Meuer, F.; Hennig, C.; Dumas, T.; Kvashnina, K.;

Originally published:

February 2023

Chemistry of Materials 35(2023)4, 1723-1734

DOI: https://doi.org/10.1021/acs.chemmater.2c03456

Perma-Link to Publication Repository of HZDR:

https://www.hzdr.de/publications/Publ-34393

From molecular oxo-hydroxo Ce clusters to crystalline CeO_2

Paul Estevenon[1,2,3], Lucia Amidani,[1,2] Stephen Bauters,[1,2] Christelle Tamain,[3] Michael Bodensteiner,[4] Florian Meuer,[4] Christoph Hennig,[1,2] Thomas Dumas,[3,*] Kristina Kvashnina[1,2,*]

[1] Helmholtz Zentrum Dresden Rossendorf (HZDR), Institute of Resource Ecology, 01314 Dresden, Germany.

[2] The Rossendorf Beamline at ESRF−The European Synchrotron, 38043 Grenoble, Cedex 9, France.

[3] CEA, DES, ISEC, DMRC, Univ Montpellier, Marcoule, France.

[4] Universität Regensburg, Fakultät für Chemie und Pharmazie, Universitätsstr. 31, 93053 Regensburg, Germany

ABSTRACT:

Due to their applications in catalysis, energy storage or biomedicine, many studies report synthesis and characterizations of CeO_2 NPs and intensively use X-ray sources for characterization. In this study, we report a comprehensive interpretation of X-ray measurements on CeO_2 models with atomically resolved structure, namely oxo-hydroxo polynuclear Ce complexes. A set of Ce clusters with growing size (0.6 nm to 1.2 nm) and nuclearity (from 6 to 38 Ce atoms) were synthetized and characterized by single crystal XRD. The samples were then analyzed using HEXS and HERFD technics and compared to larger CeO_2 NPs and bulk CeO_2. Both spectroscopic methods reveal consistent trends as the particle grows or shrink from the set of molecular Ce-{n} clusters up to bulk CeO_2. HEXS reveals a broadening in distribution for the short Ce-oxygen bonds for the small clusters. Concomitantly, the HERFD performed at the Ce L_{III} edge indicates a gradual splitting of the cerium 5d states as the particles become more CeO_2 like. From the crystallographic determination of the clusters structure, atomically resolved Ce L_{III} edge simulation were undertaken. These simulations allow to isolate structural and electronic properties for individual Ce sites within clusters and evidence the great difference between surface and core Ce atoms. It also shows how a combination of simulations from different sites results in the accurate reproduction of the corresponding experimental data. This approach based on clusters atomic sites was then successfully extended to model larger CeO_2 NPs Ce L_{III} edge HERFD spectra. By linking atomically resolved structures to nanoparticles and bulk material using crystallography, X-ray technics and simulation, this work extends the knowledge on cerium oxide nanomaterial and supports a better understanding and predictability of their crystalline and electronic structure.

Keywords: Oxo-hydroxo polynuclear complexes, HERFD, HEXS, Cerium oxide, nanoparticles, Cluster, Electronic structure, 5d

1. INTRODUCTION

Due to their strong surface redox capabilities, the CeO_2 nanoparticles (CeO_2 NPs) are very promising materials for applications in catalysis, energy storage, as surrogate for tetravalent actinide and biomedicine. [1-35] At the nanoscale, CeO_2 NPs catalytic properties are enhanced by the increase of the surface to volume ratio (S/V), which promote their reactivity. [5, 8, 18, 20, 36, 37] However the smaller the particles are, the less the crystal structure of these nanoparticles are understood since with decreasing size the percentage of surface atoms becomes relevant and the structure can differ significantly from that of bulk CeO_2 (space group $F\,m\,\bar{3}\,m$, a = 5.4097 Å) [38]. Actually, the strong structural disorder correlates to the fact that the number of surface atoms are no more negligible compared to the bulk atoms. The study of the inner structure of these particles by the conventional techniques is made difficult by the absence of long-range order and requires either crystallization of several identical particles in single crystals either the use of structural techniques that do not require long-range order and probe the atomic scale. Indeed, CeO_2 compounds have been identified with sizes ranging from nanometric species to bulk material and changes in the cerium local environment have been evidenced thanks to the High Energy Resolution Fluorescence Detected hard-ray absorption spectroscopy (HERFD-XAS).[39, 40]

On the other hand, cerium oxo-hydroxo polynuclear clusters are well defined intermediate between molecular cerium species and cerium dioxide. Indeed, the use of specific ligands and reactive conditions leads to the formation of polynuclear clusters with a cerium oxo-hydroxo assemblies surrounded by ligands. The ligand stabilizes these structures large molecular structure or may bridge oxo-hydroxo polynuclear assemblies to form Molecular Organic Framework (MOF).[41] Since these complexes can pack in single crystals, the local environment of the cerium is well known. As the cluster nuclearity increases, the local geometry of Ce atoms in the core of the clusters become close to the one reported for CeO_2.[42] This knowledge led to the hypothesis that the oxo-hydroxo clusters might be considered as elementary building blocks for the formation of bulk CeO_2 and good models to CeO_2 NPs.

Cerium (IV) oxo-hydroxo clusters have been reported with nuclearities ranging between 2 cerium atoms to 40 cerium atoms (Table 1). Among these species the hexanuclear clusters have been the most extensively studied compounds since they can form in a great variety of reactive conditions and with various ligands. Some of the largest cerium clusters may exhibit a

slightly mixed oxidation states : 2 Ce(III) atoms in Ce-{24} and 2 Ce(III) atoms in Ce-{40}; with the exception of the Ce-{38} clusters which is a pure Ce(IV) cluster.[42]

The aim of this study is to perform crossed characterization with the High Energy Resolution Fluorescence Detected X-ray Absorption Spectroscopy (HERFD-XAS), High Energy X-ray Scattering (HEXS) and single crystal X-ray diffraction (SC-XRD) to associate the Ce clusters electronic structure to the atomically resolved structure. These experiments were successfully performed on cerium cluster of 6, 24 and 38 Ce atoms and relate spectroscopic information to atomic distribution using simulation of both HEXS and Ce L_{III} edge HERFD data. A comparison with CeO_2-NPs and the corresponding Ce L_{III} edge HERFD calculations, provide a wider understanding of the nanoparticles' spectroscopic properties in relation to their probable atomic scale structure.

Table 1. Cerium polynuclear ox-hydroxo clusters reported in the literature with their core structure and largest dimension.

Nuclearity	Core structure		« Core size » (largest dimension Ce-Ce)	References
{2}	$[Ce_2(\mu_2\text{-}O)]^{6+}$		4.05–4.09 Å	43-45
{3}	$[Ce_3(\mu_2\text{-}OH)_3(\mu_3\text{-}O)]^{7+}$		3.83–3.95 Å	46, 47
	$[Ce_3(\mu_2\text{-}O)_3]^{6+}$	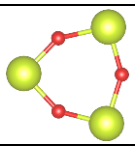	3.96 Å	46
{4}	$[Ce_4(\mu_3\text{-}O)_2]^{12+}$	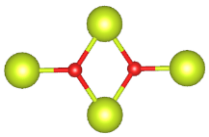	6.58–6.64Å	47, 48
{6}	$[Ce_6(\mu_3\text{-}O)_4(\mu_3\text{-}OH)_4]^{12+}$	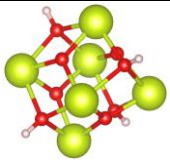	5.33–5.55 Å	46, 47, 49-56
	$[Ce_6(\mu_3\text{-}O)_5(\mu_3\text{-}OH)_3]^{11+}$		5.35 Å	57
	$[Ce_6(\mu_3\text{-}O)_8]^{8+}$	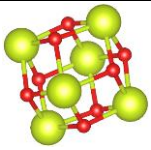	5.16–5.18 Å	53
{10}*	$[Ce_{10}(\mu_4\text{-}O)_4(\mu_3\text{-}O)_3(\mu_3\text{-}OH)]^{24+}$		7.39 Å	58
{12}	$[[Ce_6(\mu_3\text{-}O)_4(\mu_3\text{-}OH)_3](\mu_4\text{-}O)_2$ $[Ce_6(\mu_3\text{-}O)_4(\mu_3\text{-}OH)_3]]^{26+}$	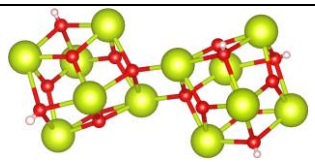	11.64 Å	59

{22}*	$[Ce_{22}(\mu_4\text{-}O)_{12}(\mu_3\text{-}O)_8(\mu_3\text{-}OH)_4]^{38+}$	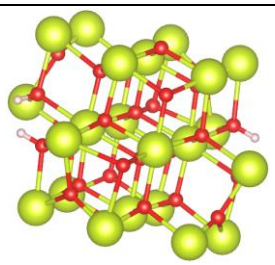	11.55 Å	58
{24}*	$[Ce_{24}(\mu_4\text{-}O)_{16}(\mu_3\text{-}O)_{12}(\mu_3\text{-}OH)_4(\mu_4\text{-}OH)_4]^{30+}$	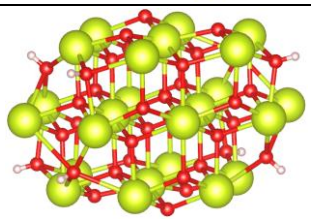	11.46 Å	42
{38}	$[Ce_{38}(\mu_4\text{-}O)_{38}(\mu_3\text{-}O)_{22}(\mu_4\text{-}OH)_6(\mu_3\text{-}OH)_2]^{24+}$	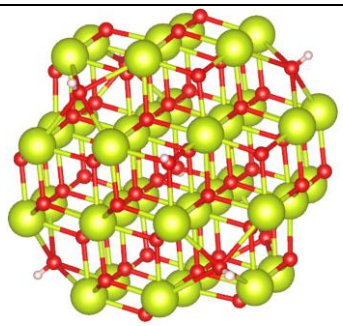	11.87 Å	42
	$[Ce_{38}(\mu_4\text{-}O)_{34}(\mu_3\text{-}O)_{24}$ $(\mu_4\text{-}OH)_2(\mu_2\text{-}OH)_8]^{26+}$	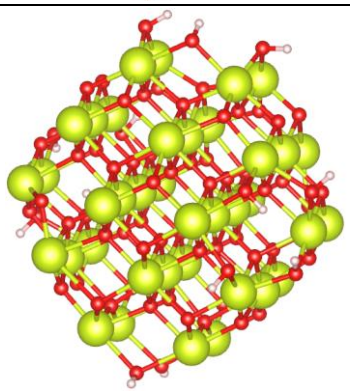	11.97 Å–12.10 Å	45, 60
{40}*	$[Ce_{40}(\mu_4\text{-}O)_{34}(\mu_3\text{-}O)_{24}(\mu_4\text{-}OH)_2]^{40+}$	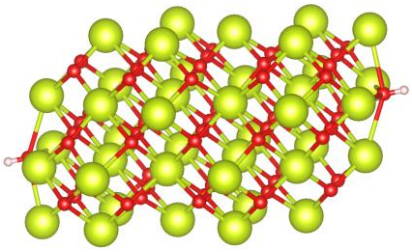	16.05 Å	42

* mixed oxidation state (Ce^{III} and Ce^{IV})

2. EXPERIMENTAL SECTION

2.1. Sample preparation

Ce(IV) in nitric acid media: nanometric $CeO_2 \cdot xH_2O$ has been prepared by addition of a cerium (IV) ammonium nitrate ($(NH_4)_2Ce(NO_3)_6$, Sigma Aldrich ≥ 98%) in deionized water on a concentrated ammoniac solution (NH_4OH, VWR 28%). The precipitate obtained was separated by centrifugation (6 min, 14.000 rpm) and washed with deionized water until the pH of the supernatant became neutral. That $CeO_2 \cdot xH_2O$ was then dissolved in nitric acid reactive media (HNO_3, VWR 65%) in order to obtain a cerium solution at 0.4 $mol \cdot L^{-1}$ at a 3 $mol \cdot L^{-1}$ acidity. The cerium oxidation state in the reactive media was fixed at +IV by electro-oxidation in galvanometric conditions (I = 1 mA) and maintained during HERFD measurements using an in-situ electrochemistry set up. The set-up is similar to the one already described by Bengio and Husar except that only the inner part of the cell was used for this experiment to provide a better HERFD signal/noise ratio.[61, 62] (The second confinement previously used for radioactive samples and dry ionic liquid was of no use for cerium aqueous electro-oxydation).

$[Ce_6(\mu_3\text{-}O)_4(\mu_3\text{-}OH)_4(NH_3CH_2COO)_9(NO_3)_6](NO_3)_6 \cdot 24H_2O$ cluster (Ce-{6}) has been prepared according to the protocol described by Estes et al.[54] by dissolving 0.985 g of $(NH_4)_2Ce(NO_3)_6$ (1.8 mmol) and 0.339 g of glycine (NH_2CH_2COOH, Sigma Aldrich ≥ 99%) (4.5 mmol) in 0.5 mL of water (27.8 mmol) in a glass vial. The solution was then put in a fridge for 2–3 days leading to the formation of the cluster. Additionally, $[Ce_6(\mu_3\text{-}O)_4(\mu_3\text{-}OH)_4(NH_3CH_2COO)_8(NO_3)_4(H_2O)_6]Cl_8 \cdot 8H_2O$ (Ce-{6}-SI-1) and $[Ce_6(\mu_3\text{-}O)_4(\mu_3\text{-}OH)_4(NH_3CH_2COO)_9(NO_3)_5H_2O](NO_3)_7 \cdot 6{-}7H_2O$ (Ce-{6}-SI-2) were prepared according to the protocol reported by Estes et al.[54] and $[Ce_6(\mu_3\text{-}O)_4(\mu_3\text{-}OH)_4(HCOO)_{10}(NO_3)_2(H_2O)_3] \cdot (H_2O)_{9.5}$ cluster (Ce-{6}-SI-3) was prepared according to the protocol reported by Hennig et al.[52]. Details of these syntheses are provided in SI. As emerged from XAS measurements, the ageing of the Ce-{6} clusters might be led to the formation of Ce(III) and to sample contamination. For this reason, only the first sample will be discussed in the main text and the other ones in supporting information.

$[Ce_{38}O_{54}(OH)_8(CH_3CH_2CO_2)_{36}(C_5H_5N)_8] \cdot 16CH_3CN$ cluster (Ce-{38}) has been prepared according to the protocol described by Mitchell et al.[42]. A mixture of 1 mL of pyridine (C_5H_5N, Prolabo ≥ 99.8%) (12.4 mmol), 100 µL of water (5.6 mmol) and 30 µL of propionic acid ($CH_3CH_2CO_2H$, Prolabo ≥ 99%) (0.4 mmol) was prepared and added on 0.055 g of $(NH_4)_2Ce(NO_3)_6$ (0.1 mmol) and 0.015 g of ammonium iodide (NH_4I, Acros Orga ≥ 98%)

(0.1 mmol) in a glass vial. The mixture obtained was stirred at 500 rpm during 30 min. Then 2 mL of acetonitrile (CH_3CN, Sigma Aldrich ≥ 99.8%) (38.3 mmol) has been added to this mixture and the solution was maintained undisturbed for several weeks leading to the formation of crystals. A closer inspection of the precipitate from the above-mentioned synthesis route with powder diffraction and a comparison with calculated powder diffractogram of the single crystal Ce-{38} suggested the presence of a second crystalline phase. Contrary to what has been reported by Mitchell et al.[42], this protocol led to the formation of Ce-{38} clusters single crystals but also to the formation of Ce-{24} single crystals which has been identified to be $[Ce_{24}O_{28}(OH)_8(CH_3CH_2CO_2)_{30}(C_5H_5N)_{7.5}]$. In the course of the investigations, this crystalline phase was identified as a Ce-{24} cluster, whose crystal structure is not yet reported. Figure 1 shows the directly measured powder data of the precipitate and the powder diffractograms of the single crystals of Ce-{38} and Ce-{24}, extracted from single crystal diffraction patterns. The 2θ range 1.3-5.0° comprises the strongest Bragg reflections. The most dominant peak at 1.9° belongs to the Ce-{38} cluster, whereas the Ce-{24} cluster reveals a prominent peak at 2.1°.

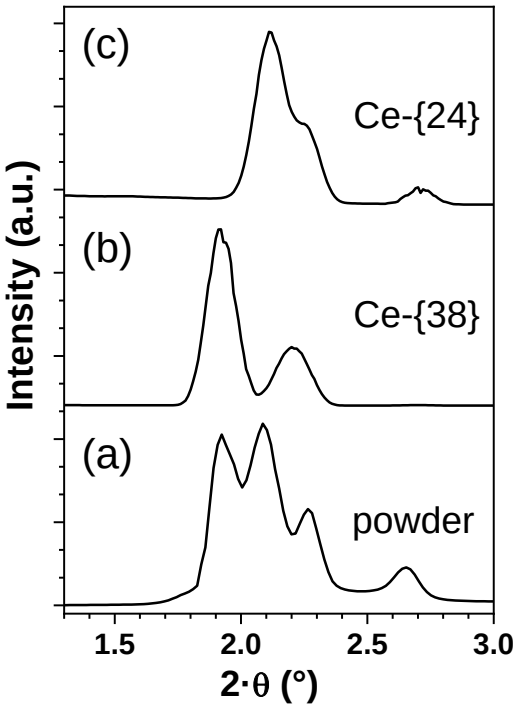

Figure 1. Powder diffraction of the precipitate (a). Powder patterns of Ce-{38} (b) and Ce-{24} (c) were extracted from single crystal diffraction data.

Attempts to obtain these clusters separately by varying the conditions (addition of acetonitrile by gas diffusion, modification of the temperature of synthesis, variation of the amount of water initially added) have been unsuccessful. Therefore, all of the Ce-{24} and Ce-{38} clusters single crystals used in this study were characterized by SC-XRD and manually separated (i.e. picking single crystal and measuring the unit cell parameters) in order to perform analyses on the separated species. However a systematic observation allowed to identify the difference of morphology between the two clusters since Ce-{38} clusters crystals are generally bigger with a square-based pyramid morphology and Ce-{24} clusters crystals are smaller with a polyhedral morphology (**Figure 2**).

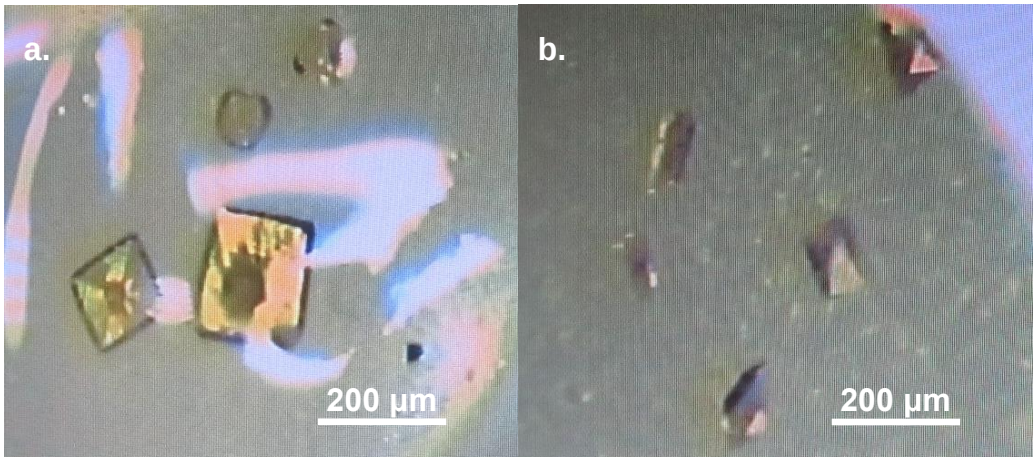

Figure 2. Pictures of Ce-{38} (a) and Ce-{24} (b) cluster single crystals.

$Ce_{38}O_{54}(OH)_8(EtCO_2)_{36}(py)_{8.25}$ (Ce-{38}) crystallizes in the space group C2/m and with the unit cell parameters a = 29.13640(10) Å, b = 28.13810(10) Å, c = 29.93190(10) Å, β = 92.26° and Z = 4. Details of the structural analysis are given in the Supporting Information. The structure of Ce-{38} (Fig. 3, left) is comprised of two different clusters in the asymmetric unit. Each cluster contains 38 Ce atoms. The Ce atoms are 8- and 9-fold coordinated. The bond valence sum (SI, Tab. 2) indicates that all Ce atoms appear in oxidation state IV. The two clusters show only minor differences in the ligand coordination. For a detailed structure description see Mitchell et al.[42] This sample was used for the XES experiments.

$Ce_{24}O_{28}(OH)_8(EtCO_2)_{30}(py)_{7.5}$ (Ce-{24}) crystallizes in the space group $P2_1/n$ and with the unit cell parameters a = 20.56554(17) Å, b = 19.84585(19) Å, c = 23.7424(3) Å, β =

90.1615(9)° and Z = 2. The scattering power of these crystals is very weak, the sample suffers radiation damage and beyond a resolution of 0.9 Å no reflections are observed. The molecular structure of Ce-{24} (Fig. 3, right) reveals one cluster in the unit cell. The core of the cluster adopts almost the same fluorite structure as CeO_2. The bond valence sums (SI, Tab. 3) show that the cluster consists of 8- and 9-fold-coordinated Ce^{4+} atoms, except for two symmetrically equivalent Ce^{3+} atoms bearing a coordination number of 10. The core cluster comprises 24 cerium atoms which are linked by 28 O^{2-}, 4 μ_4-OH^- and 4 μ_3-OH^-. The cluster coordination sphere is saturated by propionate and pyridine molecules. The former show a pronounced positional disorder over two different positions in addition to the unhindered rotation of the methyl group. The coordinated pyridine molecules are not disordered. Pyridine molecules located in the space between the clusters show partial occupation and disorder.

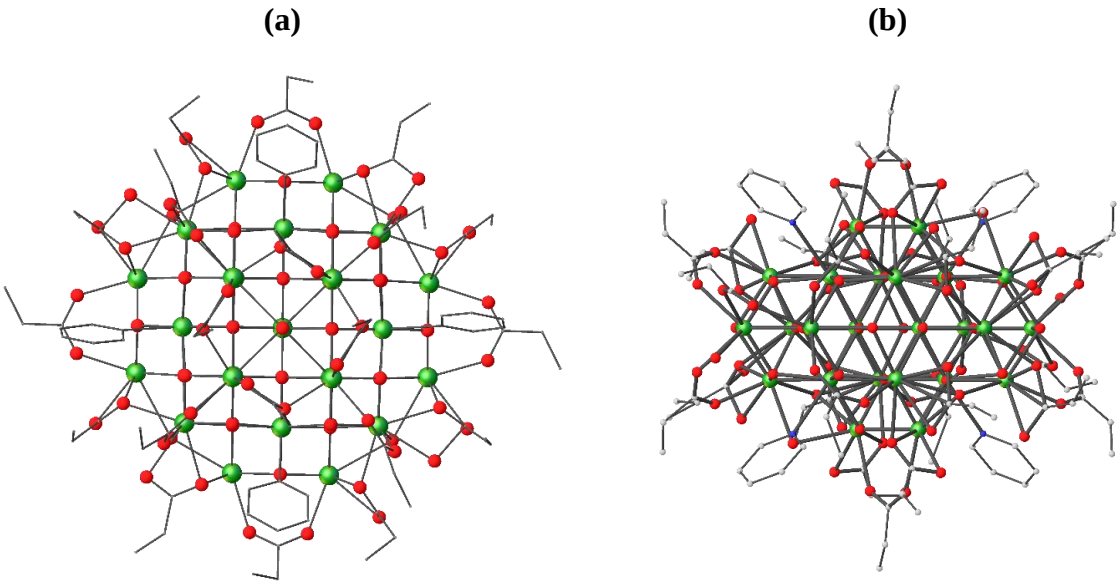

Figure 3. Structures of Ce clusters Ce-{38} (a) and Ce-{24} (b). H atoms have been omitted for clarity. Atom sizes of C is reduced to emphasize Ce and O positions. Color code: Ce green, O red, N blue, C grey.

Additionally, $[Ce_{40}O_{56}(OH)_2(CH_3CO_2)_{44}(CH_3CN)_2(C_5H_5N)_4]\cdot 48CH_3CN$ cluster (Ce-{40}) was also prepared based on the protocol described by Mitchell et al.[42]. For complementary experiments, details of this synthesis are provided in supporting information.

Bulk CeO_2 has been prepared by precipitation of cerium oxalate from cerium (III) nitrate ($Ce(NO_3)_3\cdot 6H_2O$, Sigma Aldrich, ≥ 99%) with oxalic acid ($H_2C_2O_4$, Sigma Aldrich, ≥ 98%) in

aqueous reactive media. The as precipitated cerium oxalate was separated by filtration, dried overnight at 80°C and then calcinated for 6 hours at 1200°C under air atmosphere in an open oven.

The nature of all of the Ce clusters was confirmed by SC-XRD and that of CeO_2 has been proved by PXRD.

2.2. Characterizations

SC-XRD – Each crystal was put in vacuum grease and mounted on MiTeGen microloop, inserted into a goniometer base. The single crystal XRD intensities were measured on a Bruker D8 Quest diffractometer equipped with a Photon II detector coupled device at 100 K using a 800 series Cryostream cooler (Oxford Cryosystem). The diffractometer was equipped with a Mo-target IμS Mircofocus source (λ = 0.71073 Å). Data were collected using phi and omega scans. Intensities extraction from the collected frames and structure and refinement were performed thanks to the APEX3 software. The crystal structures obtained were compared to the data available in the literature (for the Ce-{6} clusters: CCDC 925637, 1738657, 1738658 and 1738659; for the Ce-{38} cluster: CCDC 15299565; for the Ce-{40} cluster: CCDC 1529957), allowing to confirm that of the right phases were obtained.

Synchrotron SC-XRD and PXRD – The diffraction data were collected at the XRD-2 diffractometer of the Rossendorf Beamline (ESRF / Grenoble, France).[63] The beam was focused to the size of 200x200 μm^2. Experimental data were collected using the Pyatus software.[64] The detector geometry parameters of the Pilatus3 X 2M detector were calibrated with PyFAI [65] using the NIST standard LaB_6.

The powdered precipitate of sample Ce-{38}/Ce-{24} was measured using an excitation energy of 22000eV (wavelength 0.56356Å) at ambient temperature. The data were extracted with the BUBBLE software.[64] This diffractogram was compared with data from single crystals selected from the precipitate. Single crystals of Ce38 and Ce24 were measured using the same energy with a phi scan of 360°, angular steps of 0.1° and a counting time of 0.1s per frame. The powder diffractograms of the single crystals were extracted with powder integration module of CrysalisPro (Crysalis Pro V.40 Rigaku Oxford diffraction).

The single crystal structures were determined from a set of omega scans using a Huber Kappa goniometer at an excitation energy of 20043eV (wavelength 0.61862Å). The

measurements were performed at 100K in shutterless mode, an angular step size of 0.1° and a counting time of 0.1s per frame. The data were treated with the SNBL ToolBox [64] and Crysalis Pro. The disordered positions were refined using geometrical and displacement constraints and restraints.

HERFD – The experiments were performed at beamline BM20 of the European Synchrotron Radiation Facility in Grenoble.[63] The incident energy was selected using the <111> reflection from a double Si crystal monochromator. Rejection of higher harmonics was achieved by two Si mirrors working at an angle of 2.5 mrad relative to the incident beam. HERFD-XAS spectra were measured using an X-ray emission spectrometer [66] at 90° horizontal scattering angle. Sample, analyser crystal and photon detector (Ketek) were arranged in a vertical Rowland geometry.

The Ce HERFD-XAS spectra at the L_{III} edge were obtained by recording the maximum intensity of the Ce $L\alpha_1$ emission line (4839 eV) as a function of the incident energy with five spherically bent crystal analysers. The emission energy was selected using the <331> reflection of five spherically bent Ge crystal analyser (with R = 1m) aligned at a 87° Bragg angle. The size of the beam at the sample was 350 μm horizontal times 100 μm vertical. A combined (incident convoluted with emitted) energy resolution of 0.8 eV was obtained, as determined by measuring the FWHM of the elastic peak.

Samples for the HERFD-XAS measurements were prepared as wet pastes and sealed with single kapton confinement.

HEXS – The data on Ce-{6}, Ce-{38} and CeO_2 were collected on at the ID15A beamline [67] of the European Synchrotron Radiation Facility (ESRF, Grenoble). The data were collected at room temperature, the incident energy was set to 100 keV and we measured up to 30 $Å^{-1}$ using a Dectris CdTe 2M pixel detector. The samples were sealed in 1 mm diameter quartz capillaries and the signal from an empty capillary was used for background subtraction. Patterns were corrected for detector geometry, response and transparency, and integrated by using a locally modified version of pyFAI [68] with outlier filtering. The PDF was calculated from the resulting powder diffraction patterns by using modules from PDFgetX3 [69] and the data were corrected for electronic noise and weak spurious signals by fitting the high-angle part of the calculated F(q) to a weighted spline to remove outliers following a procedure similar to that described previously.[70] The PDF Gaussian dampening envelope due to limited Q-resolution and Q-broadening was obtained from the fit of a reference sample and fixed at these values for the

NPs. The maximum scattering vector Q of the data used for the generation of the PDF was 26 $Å^{-1}$. PDF of Ce-{6} and Ce-{38} were calculated with the DebyePDFCalculator implemented in diffpy-CMI [71] starting from published structures of Estes and Mitchell.[42, 54] The PDF measured for the Ce(IV) solubilized in nitric acid is compared to crystal structures that include a linear Ce-μ_2O-Ce bridge (Table 1).[43-45]

2.3. Theoretical Ce L_{III} edge simulations

The Ce L_{III} theoretical calculations were performed using the FEFF 9.4. code.[72] The input files were made from a cif file using the sub-program of the Demeter software ATOMS. The atomic coordinates used as input for HERFD calculations were obtained from reported XRD structures, including the CeO_2 for which the atomic unit cell parameter a = 0.541 nm were applied. Calculations were made in a similar way, as reported by Li et al. [73] previously for bulk CeO_2 and by Plakhova et al. for CeO_2 NPs.[39]

Full multiple scattering (FMS) calculations were performed using a Hedin–Lundqvist self-energy correction and other standard cards. The apparent reduction of the core-hole lifetime broadening was achieved by using the EXCHANGE card and core electron were unfreezed using the UNFREEZREF card as it is necessary for element accurate calculation.

For the Ce(IV) dimers the structure origins from the $Ce_2(\mu_2\text{-}O)(NO_3)_6(H_2O)_6 \cdot 2H_2O$ [45] structure and both Ce atoms were considered equivalent. It is also the case for the 6 cerium atoms in the Ce-{6} glycine simulation and for bulk CeO_2. In contrast, the Ce-{38} cluster consists in a more complicated geometry and overall at least 3 different types of Ce atoms must be considered. 6 Ce core atoms are CeO_2 like and “see” 12 other Ce atoms in the second coordination shell. 8 intermediate corner sites are incomplete bulk-like sites that “see” only 9 Ce atoms in their second coordination shell. And finally, the surface Ce atoms that “see” only 7 Ce atoms in their second coordination shell. The full Ce-{38} spectrum is produced by the addition of the 6/38 of the bulk spectrum, 8/38 intermediate and 24/38 surface spectrum.

3. RESULTS AND DISCUSSION

3.1. HEXS

The structure of nanosize systems can be probed thanks to HEXS measurements, which measures the arrangement of atoms with angstrom resolution without requiring long-range

order, such as XRD characterization, thereby making it suitable for the characterization of amorphous and nanostructured systems.[74-76] From HEXS the pair distribution function (PDF) can be extracted, which is an appropriately normalized Fourier transform of the total scattering signal and provides the probability of finding a pair of atoms separated by a specified distance. Using this technique for the characterization of cluster samples provides a useful insight into the evolution of the structure from clusters to bulk CeO_2. In our case the structures are known from the single crystal XRD and experimental data can be compared with PDF calculated from the known structures.

In **Figure 4**, the PDF data for the Ce-{2} Ce-{6} and Ce-{38} clusters are compared to the CeO_2 one. The PDF calculated for Ce-{6} and Ce-{38} from reported structures are also shown together with the histograms of Ce-centered distances. The PDF was also measured for the Ce(IV) solubilized in nitric acid (named Ce-{2}). The almost flat signal (besides broad oscillations between 2 and 2.4 Å due to Ce-O bonds) still allows the observation of a small contribution around 4.0–4.1 Å. This is the Ce–Ce distance proposed previously for dimeric cerium clusters from EXAFS measurements and is well reproduced by the simulation. From PDF data the progressive increase of the core is readily seen as the presence of peaks at longer distances. Due to the large differences in scattering power between Ce and the lighter atoms forming the cluster, peaks due to distances between Ce and other atoms dominate the signal and the most intense correspond to Ce – Ce pairs. The Ce-{6} cluster presents two characteristic Ce–Ce distances around 3.78 and 5.35 Å[54] whose peaks are clearly visible in the PDF signal. Similar results were obtained on analogous hexanuclear compounds prepared with either glycine or formic acid ligands (**Figure S13**). The PDF data for the Ce-{38} cluster shows longer Ce–Ce distances up to 11.5 Å, in good agreement with the expected values from the Ce-{38} crystal structure (**Table 1**).[42] The PDFs calculated from the reported structured for Ce-{6} and Ce-{38} reproduce very well the experimental data, a further confirmation of the correctness of the structures. Overall, it is observed that the increase of the cluster core size results in PDF closer to that of the CeO_2.

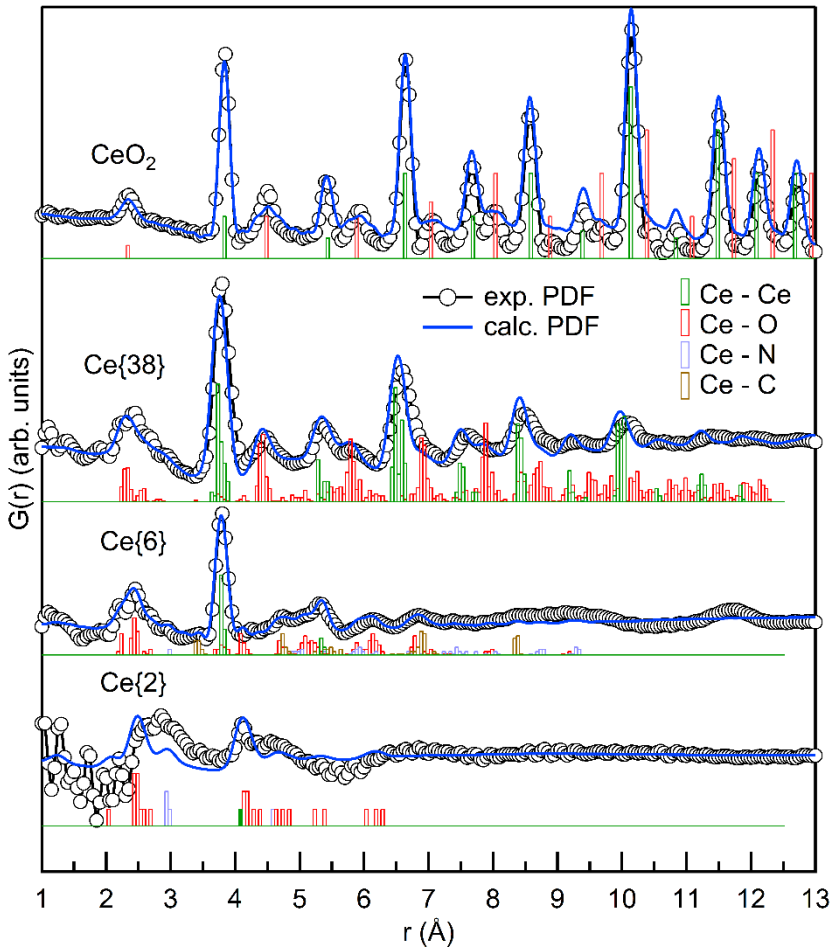

Figure 4. Unscaled PDFs for the Ce-{2}, Ce-{6} cluster, Ce-{38} cluster and bulk CeO_2 samples in the 1–13 Å range. PDF experimental data (black circles) are compared to calculated PDFs for a single cluster motif (blue line). The vertical sticks at the bottom indicate the theoretical cerium centered pair distances.

An important difference however can be readily observed between clusters and bulk CeO_2. For clusters, both the experimental and modeled PDF show a splitting of the first peak corresponding to Ce – O distances. Indeed, for both Ce-{6} and Ce-{38}, the first peak signal extends between 2 and 3 Å and shows three contributions in contrast to the single peak observed for CeO_2. Indeed, in CeO_2, there is only a single Ce μ_4-O bonds at 2.34 Å,[38] whereas for clusters different Ce – O distances are found reflecting the local disorder at the surface. For Ce-{6}, all Ce atoms can be considered surface atoms and indeed each of them presents three different Ce – O distances: the shorter around 2.2 Å corresponding to bonds with μ_3-O atoms, the longer around 2.63 Å corresponding to OH groups and several distances around 2.4-2.5 Å

corresponding to μ_3-OH atoms and to O atoms connected to decorating functional groups.[54] For the Ce-{38} cluster a similar splitting of the first peak is observed. Analysis of the structure reveals that a single Ce – O distance around 2.34 Å characterizes core Ce atoms, while for Ce at the surface longer bonds are found around 2.55 Å with O of the decorating functional groups. This effect on the first coordination sphere was already evidenced for f-elements oxo-hydroxide materials using EXAFS for both clusters and nanoparticles.[77-79] Therefore, it is interesting to notice this effect which is a reliable footprint of the relevance of surface atoms in a nanostructure and can be easily measured with HEXS. It is expected that the bigger is the nanoparticle (i.e. low S/V ratio), the more the first peak is converging to the shape of CeO_2 due to the increasing number of core atoms for which a single bond distance is found.

Ce L_{III} HERFD

The cerium (IV) clusters were characterized by HERFD-XAS at the cerium L_{III} edge (**Figure 3**). The cerium oxidation state in these samples was checked on the basis of the cerium pre-edge (around 5718 eV), peak A on the **Figure 3**, originating from the electronic transition from 2p to 4f valence orbitals.[80] Each cluster was compared to samples with pure oxidation state: a monazite sample, $CePO_4$, for Ce(III), a Ce^{4+} aqueous solution in nitric acid media (maintained by electro-oxidation) and a CeO_2 sample standing for Ce(IV) (inserts in Figure 2). This comparison allowed to confirm that cerium is mainly at the oxidation state +IV for all the samples considered, since no intensity raise belong to the Ce(III) species has been found at the energy of 5715.5 eV. Moreover, the Ce(IV) solution and the cerium dioxide were used as references in order to estimate the impact of the cluster nuclearities on the shape of their HERFD spectra. The Ce(IV) in aqueous solution exhibited a spectrum with two main peaks centered around 5726.6 eV and 5737.0 eV, peaks B and C on the **Figure 3**. These peaks are coming from electron transition from $2p_{3/2} \rightarrow 5d_{5/2}$ states and could be assigned to the screened (B) and unscreened (C) excited states.[81-84] A splitting of these peaks could be observed for the CeO_2 spectrum (peaks B_1 and B_2 and peaks C_1 and C_2 on the **Figure 3**).[83, 84] That splitting is an effect of the crystal field in the CeO_2 fluorite structure where each cerium atom is surrounded by 8 oxygen atoms with an O_h point symmetry group.[40, 85] It leads to the observation of two groups of two peaks, a first one where the peaks are located around 5724.5 eV (B_1) and 5728.4 eV (B_2) and a second one where they are located around 5735.9 eV (C_1) and 5738.5 eV (C_2). Indeed, due to the cubic crystal field, the Ce^{IV} $5d^0$ configuration is split into the e_g and t_{2g}

bands corresponding to B_1 – C_2 (screened and unscreened) and B_2 – C_1 (screened and unscreened) peaks respectively.

From this basis, it was observed that the Ce-{6} cluster (**Figure 5a**) exhibits a shape very similar to the one of the Ce(IV) in aqueous solution, with a slight broadening of the peaks B and C. These clusters exhibit short μ_3 oxygen atoms and a structure where the local geometry around the cerium atoms is similar to that of surface cerium atoms of larger Ce clusters (i.e. Ce-{24} and Ce-{38}).[42] For this reason, these hexameric clusters might be considered as the first step of the Ce(IV) hydrolysis. However, despite these structural properties, the HERFD spectra for these compounds are quite far from that of the oxide, without any significant splitting of the B and C peaks. On the opposite, the larger cerium clusters Ce-{24} and Ce-{38} (**Figure 5b** and **Figure 5c** respectively) exhibit HERFD spectra which are intermediate between the spectra reported for aqueous Ce(IV) and CeO_2. An important broadening of the two characteristic Ce(IV) peaks (B and C) was observed for these spectra with a shoulder on the B peak at lower energy and another shoulder on the C peak at higher energy, respectively corresponding to B_1 – B_2 and C_1 – C_2 splits (screened and unscreened states are always split in the same manner [81]). This evidence of a peak splitting effect similar to the crystal field splitting in the CeO_2 fluorite structure. Moreover, if we consider the peaks maxima, when the cluster nuclearity increases, the B peak maximum (B_2) shifts to higher energy, the C peak maximum (C_1) concomitantly shifts to lower energy. Altogether, the trend is a splitting of both B and C peaks to approach the CeO_2 spectral shape as the cluster size increases. This effect of the B and C peaks depending on the size of the nanoparticles was previously observed by Paun et al[85] in experiments ranging from 2 nm to 11 nm particle size. The authors also proposed that Ce L_{III} HERFD simulation may reproduced this size-dependent changes in the B peak shape.

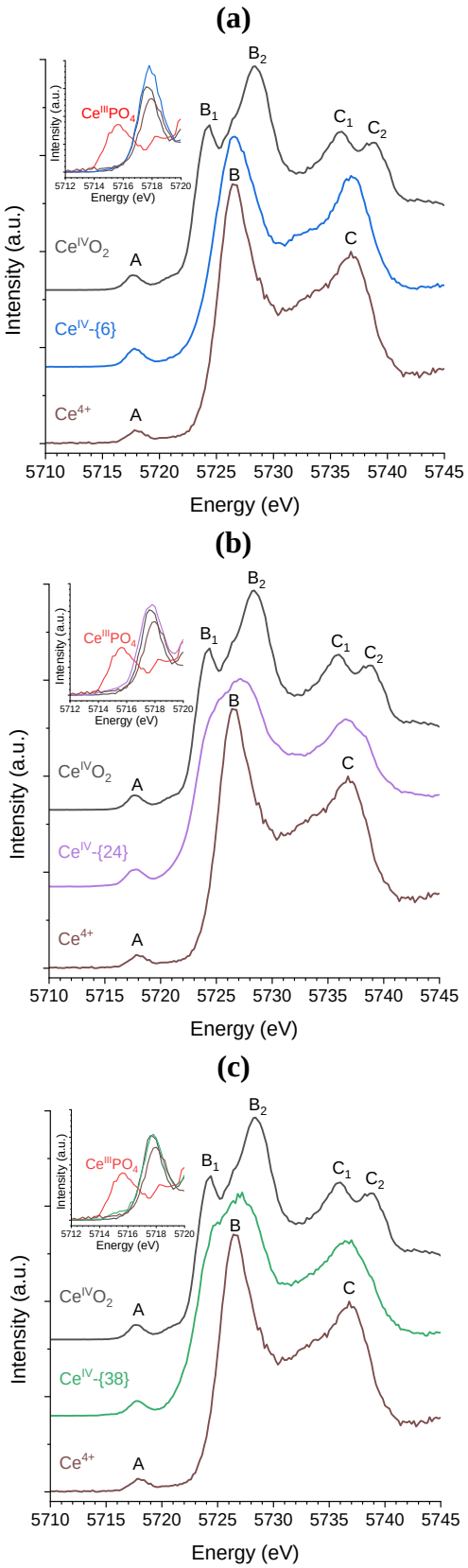

Figure 5. HERFD-XAS spectra at Ce L_{III} edge for the Ce-{6} (a), Ce-{24} (b) and Ce-{38} (c) clusters compared to aqueous Ce^{4+} and bulk CeO_2 references. The magnification of the pre-edge was reported in the inserts and compared to monazite as Ce(III) oxidation state reference.

Ce L_{III} HERFD simulation and comparison to CeO_2 NPs

Many other experimental studies report a splitting of the B and C peaks of the HERFD-XAS spectra for CeO_2 NPs.[39, 40] In that perspective, we propose a comparison between this work results and 2 nm and 8 nm CeO_2 NPs recently reported in the literature by Plakhova et al. (**Figure 6a**).[39, 40] Due to their size (see Table 1: the longer Ce-Ce distances in the Ce-{24} and Ce-{38} are 11.46 Å and 11.86 Å respectively), the larger Ce oxo-hydroxo clusters are intermediate states of the growth of the oxo-hydroxo NPs. Meanwhile, the peak B and C splitting observed at the clusters Ce L_{III} edge is also showing an intermediate shape between larger CeO_2 nanoparticles and molecular Ce^{4+} compounds. The Ce-{6} only shows a broadening of peak B and C. To understand the shape of clusters spectra, we took advantage of the cluster XRD structure to simulate Ce-L_{III} spectra as a function of (1) the structure of the cluster and (2) the individual atomic position of the absorbing cerium atom. For the sake of comparison, the simulated spectra to both aqueous Ce(IV) and CeO_2 are also presented (**Figure 6b**).

Here, we only compare the first part of the absorption spectra corresponding to 2p−5d transitions (peak $B_{1,2}$). Peak C is not simulated by the monoelectronic FEFF code approach nor discussed here since it involves multi-electronic excitations but the crystal field splitting behavior of the unscreened states C remains the same as for the states B. Therefore, our analysis focuses on the shape of peak B. As for the experimental spectra, the simulation clearly distinguishes between the molecular Ce(IV) and the periodic CeO_2 spectra. On the experimental dataset, the intermediate cluster and CeO_2 NP's from Plakhova et al.[39, 40] nicely match in between the large clusters and CeO2. It has been clearly demonstrated that the CeO_2 B peak splits due to the crystal field in the CeO_2 fluorite structure.[40, 85] The 8 coordinated Ce atoms in CeO_2 belongs to the O_h point group leading to a splitting of Ce 5d orbitals in two groups, i.e. e_g and t_{2g}. As in previous studies,[40, 85] this effect is nicely reproduced by the calculations and results in two main groups of transition. The first one corresponds to a less intense transition to e_g orbitals (experimentally B_1) and the second to more intense transitions to t_{2g} (experimentally B_2). In contrast, the Ce(IV) ions in nitric acid solution form a distorted 9 fold trigonal tricapped coordination polyhedron resulting in a single transition to 5d orbitals. The resulting spectrum is made of a single peak that also well correspond to the experimental B peak for the corresponding experiment. Considering now clusters, the Ce atoms in the Ce-{6} cluster belong also to a 9 fold coordination polyhedron but this time with a spread Ce-O bonds distances ranging between 2.2 and 2.7 Å. The result is a broadening of 5d state density (see **Figure S20**

for a detailed DOS description). However, this still results in a single broad peak in agreement with the experimental measurement, due to the core-hole lifetime broadening of the Ce L_{III} edge. For the Ce-{38} cluster, one needs to distinguish 3 types of Ce atoms from the surface to the core of the cluster (**Figure S14** and **Figure S15**). The surface atoms are 9 folded (**Figure S15**), Ce-O bonds ranges between 2.2 and 2.8 Å and, in a sense, are similar to the Ce-{6} cluster Ce site. The Ce coordination is even more distorted and the calculations predict an important broadening of 5d state density (**Figure 6b blue spectrum**). While moving into the core of the cluster, intermediate and core sites become more similar to the CeO_2 structure. For the intermediate sites the Ce atoms are 8-fold and Ce-O bonds range between 2.25 Å and 2.35 Å with a Ce-$N_{pyridine}$ bound of 2.73 Å. For the core like site, Ce atoms are 8-fold and Ce-O bonds range between 2.31 Å and 2.34 Å. Calculations performed on these individual sites show the separation of the Ce 5d DOS resulting on the split in the corresponding spectra. While the geometry is not quite as symmetrical as in the CeO_2 structure (O_h), the calculations for core like atoms become close to it and explain the experimentally observed B_1-B_2 split for large cluster samples. Overall, the Ce-{38} spectrum is made of the combination of the 3 sites. This results in a spectrum that reproduces well experimental peak B. For the other cluster size (Ce-{24} and Ce-{40}), the same 3 sites are still present but different surface, intermediate and core sites ratio that results in a progressive change in the B_1 and B_2 split.

(a)

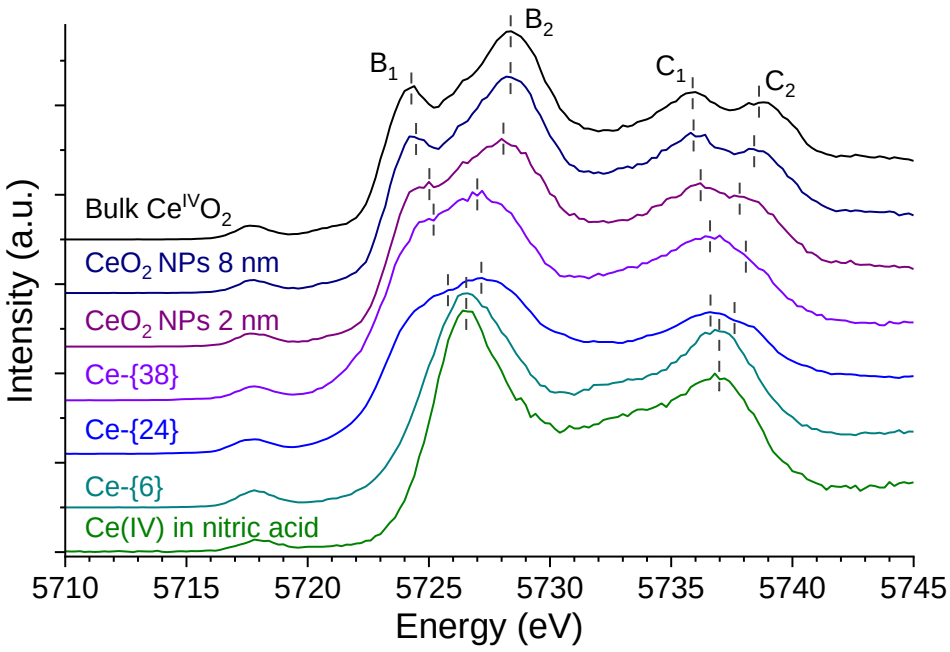
B1
B2
C1
C2
Bulk Ce^IVO2
CeO2 NPs 8 nm
CeO2 NPs 2 nm
Ce-{38}
Ce-{24}
Ce-{6}
Ce(IV) in nitric acid
Intensity (a.u.)
5710
5715
5720
5725
5730
5735
5740
5745
Energy (eV)

(b)

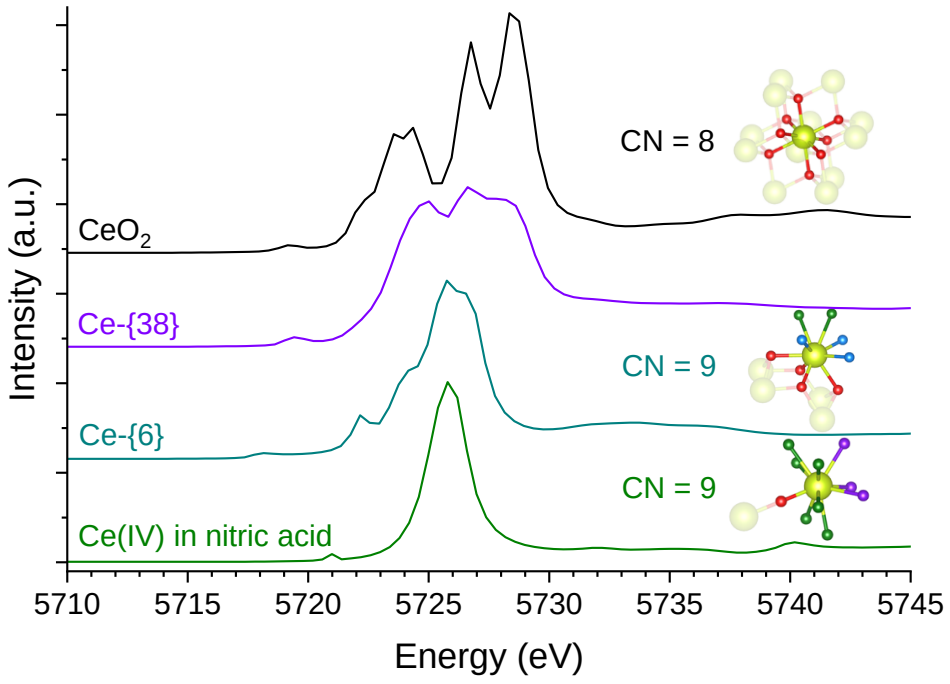
CN = 8
CeO2
Ce-{38}
CN = 9
Ce-{6}
CN = 9
Ce(IV) in nitric acid
Intensity (a.u.)
5710
5715
5720
5725
5730
5735
5740
5745
Energy (eV)

(c)

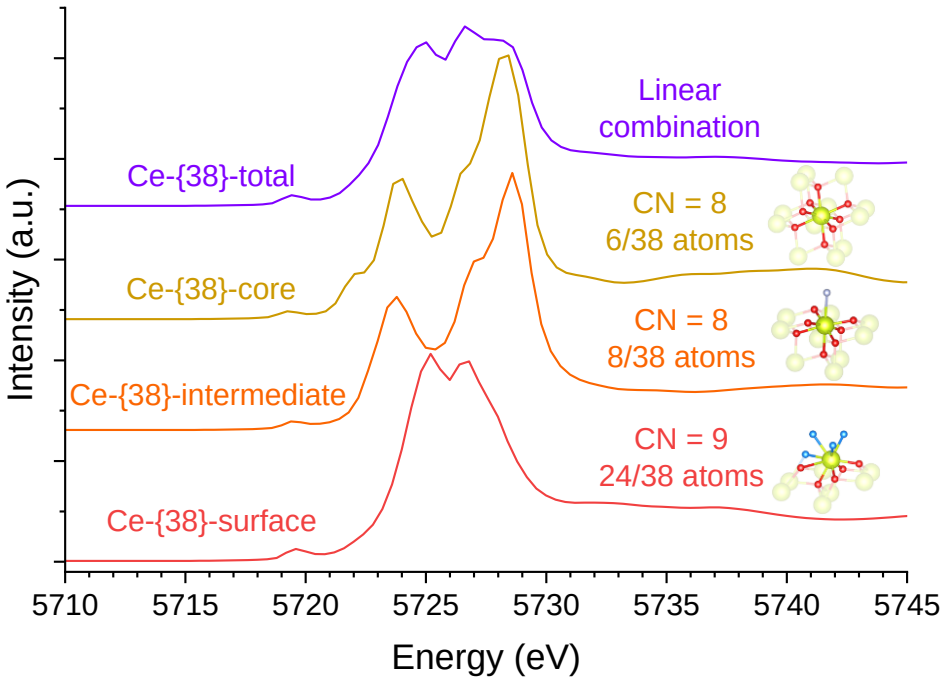

Figure 6. HERFD spectra at Ce L_{III} edge for aqueous Ce^{4+}, Ce-{6}, Ce-{24}, Ce-{38} and bulk CeO_2 compared to 2nm and 8 nm CeO_2 nanoparticles, data reproduced from 39, 40 (a), simulated spectra for Ce(IV) dimers in nitric acid, Ce-{6}, Ce-{38} and CeO_2 (b) and the linear combination leading to the Ce-{38} simulated spectrum (c).

Along the series of cluster compounds, the B_1-B_2 split propagates as the number of core atoms increases in front of the surface ones. This effect is experimentally extended to the larger CeO_2 NPs **Figure 6a**. This spectral modification at Ce L_{III} edge has been already observed for NPs and considered as a nanosized effect on the Ce O_h crystal field.[39, 40, 85] Our analysis of large clusters electronic structure, allowing an individual atomic sites calculation, depicts more precisely how the core and surface Ce atoms entanglement impact the electronic structure of these materials. From these atomically resolved compounds and the corresponding Ce L_{III} edge calculations, the B_1 to B_2 split originates only from bulk atoms while the modification from a standard CeO_2 material belongs to the surface Ce atoms that become predominant as the particle size decreases.

From this idea, an empirical relation between the 5d states electronic structure and the particle size may be drawn. As the peak positions can be determined from the derivative of the sample's spectra, the difference of energy $E_{B2} - E_{B1}$ was calculated for every samples. This parameter was called Δ_{Oh}. These values were gathered in **Figure 7** as a function of the ratio of

core cerium atoms against the total number of cerium atoms in the cluster/nanoparticle. In order to define this parameter in cerium clusters, we identified core cerium atoms to be Ce atoms with a square prismatic configuration (i.e., Ce atoms octa-coordinated with a square antiprismatic configuration and nonacoordinated Ce atoms were not considered to be core cerium atoms):

- Ce-{6}: $Ce_{core}/Ce_{total} = 0/6 = 0$;
- Ce-{24}: $Ce_{core}/Ce_{total} = 6/24 = 0.25$;
- Ce-{38}: $Ce_{core}/Ce_{total} = 14/38 \approx 0.368$.

Regarding the CeO_2 NPs, the Ce_{core}/Ce_{total} ratio was calculated geometrically by considering the NPs to be spheres with a single size distribution (with an uncertainty associated D(10) and D(90) determined for these nanoparticles), the cerium atoms to be homogeneously distributed in the particle and the cerium atoms which didn't correspond to core atoms located on an outer sphere layer at 2.3 Å from the surface (corresponding to a typical Ce-O distance in CeO_2 [38]). These approximations led the ratio calculated to be:

$$\frac{\mathrm{Ce_{core}}}{\mathrm{Ce_{total}}} = \frac{\mathrm{V_{inner\ sphere}}}{\mathrm{V_{particle}}} = \frac{(\mathrm{R} - 0.23)^3}{\mathrm{R}^3}$$

With R corresponding to the NPs radius in nm.

- CeO_2 NPs 2nm: $Ce_{core}/Ce_{total} \approx 0.457$;
- CeO_2 NPs 8nm: $Ce_{core}/Ce_{total} \approx 0.837$;
- CeO_2 core: $Ce_{core}/Ce_{total} \approx 1$.

From these data, a linear relationship was established: $\Delta_{Oh} = 4.629 \times \frac{\mathrm{Ce_{core}}}{\mathrm{Ce_{total}}}$, with a linear regression coefficient of $r^2 = 0.97$ (**Figure 7a**). That relationship evidenced the correlation between the CeO_2 NPs size and the Δ_{Oh} parameter. However, it might be observed that this relationship led to an underestimation of the Δ_{Oh} parameter for the 2 nm NPs compared to the experimental values and to an overestimation of that parameter for the largest CeO_2 particles.

Moreover, that relationship is very dependent to the definition provided for the core cerium atoms, especially for the CeO_2 NPs, since decreasing the thickness of the surface layer would modify the point position. Indeed, in the current case, considering a thicker surface layer (i.e. 1.0 Å, **Figure 7b**), led to a better correlation coefficient, despite that definition might be difficult to correlate to physical results. These results suggest that it might be a bias in the evaluation of NPs size depending on the equation considered and additional points for different particles size might be required to evaluate the regression coefficient with a better accuracy.

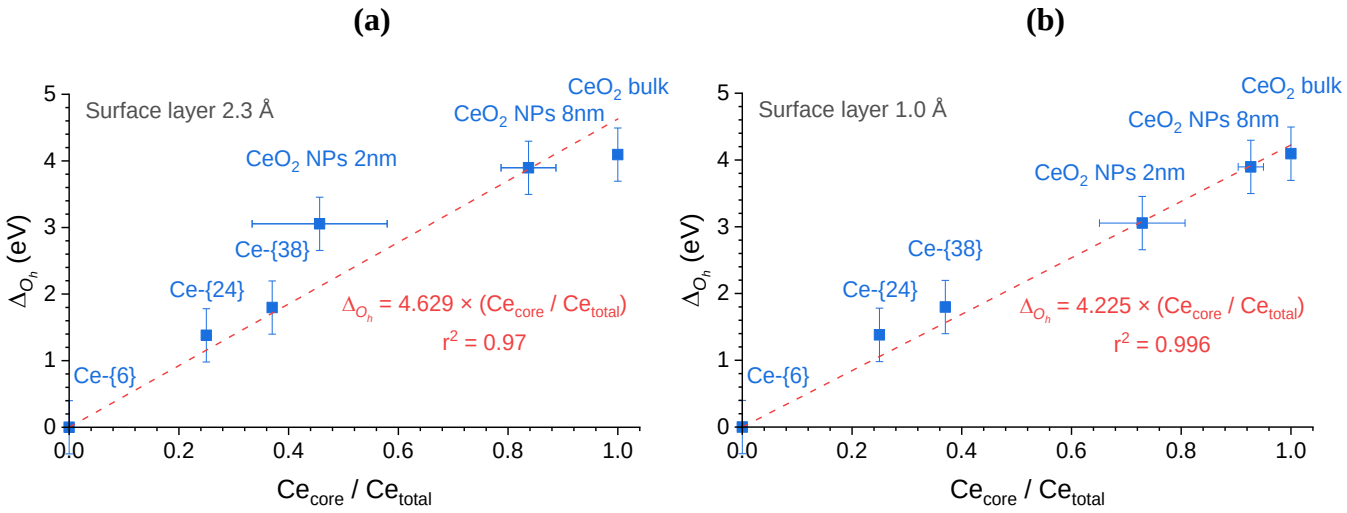

Figure 7. Δ_{Oh} parameter depending on the Ce_{core}/Ce_{total} ratio for 2.3 Å (a) and 1.0 Å (b) surface layers.

In order to avoid any bias on the evaluation of the NPs size depending of the definition chosen for CeO_2 NPs surface layer, we decided to simulate the CeO_2 NPs spectra thanks to the data obtained for Ce-{38} core and surface atoms by the monoelectronic FEFF code approach. The spectra were calculated to be a linear combination of Ce-core and Ce-surface atoms contribution (with the same definition as the one provided previously). The calculation performed for Ce-{38} cluster allowed us to observe that the experimental value of Δ_{Oh} can be replicate by this approach (**Figure 8**). Moreover, the calculated spectrum for the Ce_{core} atoms also allowed to simulate correctly the bulk CeO_2 Δ_{Oh}. Simulating the CeO_2 NPs spectra from that approach provide the red curve provided in **Figure 8**. It might be observed that these results are in good agreement with the experimental points obtained by supposing the surface layer thickness to be equal to one Ce-O distance (2.3 Å) and are also in good agreement with the values obtained for large Ce-clusters (Ce-{24} and Ce-{38}. However, the spectrum calculated for surface Ce atoms provides a Δ_{Oh} value which is not correspond to the one experimentally obtained for Ce-{6} clusters. Nevertheless, these results allowed to suppose that this approach provides good evaluation of CeO_2 NPs particle size for particles larger than 1 nm.

Evaluation of particles size for the CeO_2 NPs model proposed is gathered in Supporting information in **Table S7**.

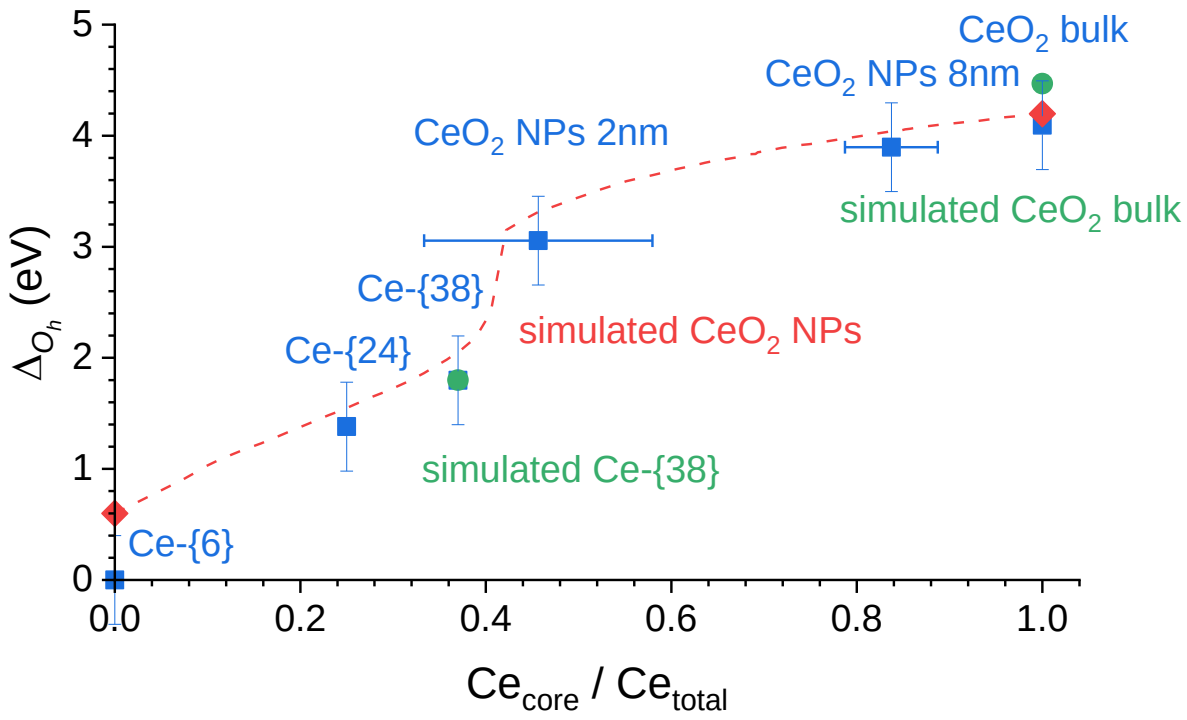

Figure 8. Δ_{Oh} parameter depending on the Ce_{core}/Ce_{total} ratio for 2.3 Å surface layer thickness (in blue), Δ_{Oh} evaluated from monoelectronic FEFF code approach calculation for Ce-{38} (in green) and CeO_2 NPs (in red).

A difference between B and C peaks Δ_{Oh} was also evidenced by our experiments. However, C peaks couldn't be simulated by the same approach we used for B peaks.

Since the C peak split is also affected by the O_h crystal field, the energy difference $E_{C2} - E_{C1}$ were gathered in **Figure 9.** as a function of the Ce_{core}/Ce_{total} ratio. The comparison with the values obtained for Δ_{Oh} evidenced a difference between the B and C peaks behavior. Indeed, significant differences in energy splitting were evidenced. A pseudo-linear relationship might also be extracted from those data, allowing to evaluate the size of CeO_2 NPs from the C peak splitting:

- $E_{C2} - E_{C1} = 2.712 \times \frac{Ce_{core}}{Ce_{total}}$; $r^2 = 0.976$; if we considered a 1.0 Å surface layer
- $E_{C2} - E_{C1} = 3.017 \times \frac{Ce_{core}}{Ce_{total}}$; $r^2 = 0.984$; if we considered a 2.3 Å surface layer

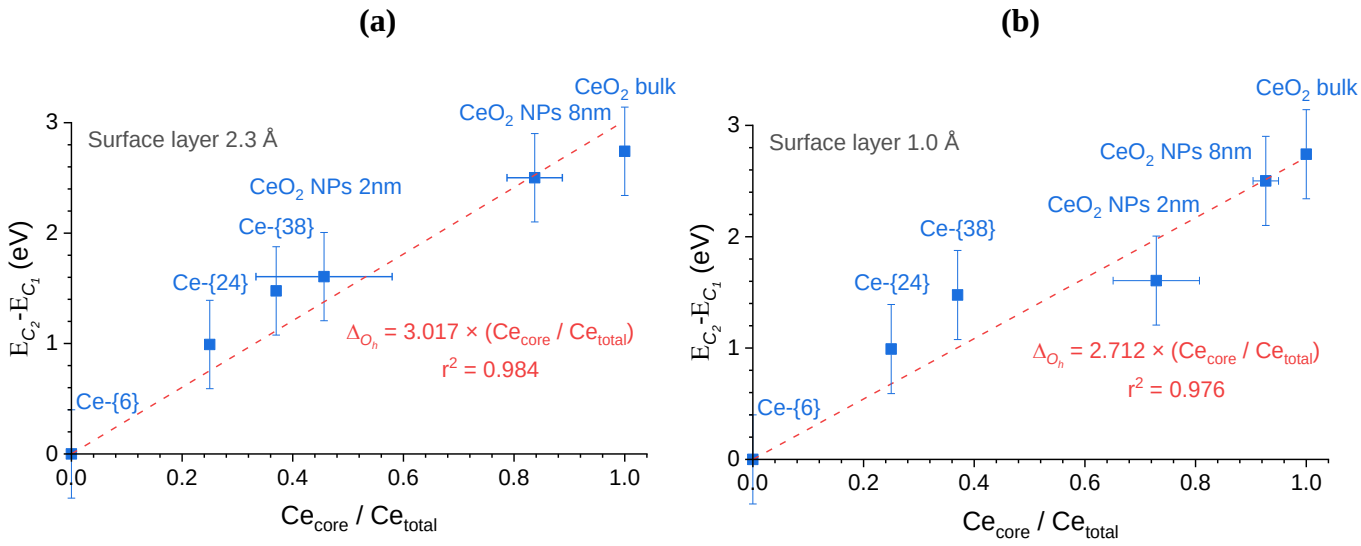

Figure 9. $E_{C2} - E_{C1}$ parameter depending on the Ce_{core}/Ce_{total} ratio for 2.3 Å (a) and 1.0 Å (b) surface layers.

Contrary to the results obtained for Δ_{Oh} the linear approximation for 2.3 Å surface layer seems to provide a finer correlation with the experimental values. However, since the value of the surface layers experimented were arbitrary chosen, it is difficult to conclude from this point. Moreover, since the C peaks result could not be simulated (due to single-electron FEFF approximation), these empirical relationships are the only ones allowing to get an evaluation of the particle size. Nevertheless, the crossing approach from the evaluation of B and C peaks splitting would allow to improve the precision of the particle size evaluation.

However, experimental limitation might be associated with the determination of these empirical relationships which emphasis the uncertainty of this empirical approach that belongs to a few factors: (i) in some cases the signal / noise ratio may impede the ability to define accurately a peak maximum energy (ii) the identification of the B peak splitting might be heavily affected by the presence of Ce(III) in the samples, because of the trivalent cerium white line at 5723.8 eV (**Figure S9, S10, S11 and S12**). (iii) the C peak splitting is smaller and harder to identify than the B peak splitting particularly for very small particles, however, it is not affected by the presence of Ce(III) in the sample (Ce(III) spectra never contains multi-electron excitations) (iv) the particle shape (assumed in this work to be spherical; see description in supporting information) and surface roughness might influence the Ce_{core}/Ce_{total} value (v) the differences of energy parameter obtain for B and C peaks for NPs larger than 8 nm is too close to the HERFD resolution to be significant and results to a limitation of the accurate particle size

determination for bigger NPs (vi) finally the presence of surfactants of the outer shell formation in NPs (like hydroxy groups shell), might affect the HERFD spectra shape. Nevertheless, applied with care, these relationships might allow to estimate in-situ the median size of colloidal particles from HERFD-XAS spectra which may provide useful hints for future studies. In addition, this approach will benefit Ce L_{III} data analysis in mixed oxides wherein the CeO_2 L_{III} spectra is often applied solely in linear combination fits. While this allows a first rough approximation of the cerium redox state, [40] the combination of surface and core Ce L_{III} spectra proposed in this work should improve this evaluation by assigning properly the experimental B_1-B_2 and C_1-C_2 splits.

4. CONCLUSION

Cerium oxo-hydroxo NPs structural properties and electronic structure are important for many applications and are extensively studied. Both properties are probed using complementary technics often based on X-ray methods. In this this work we focus on HEXS and HERFD-XAS. This work purpose was to link these measurements to an atomic scale description by using structurally defined standards. We selected and synthesized as a single crystal a set of cerium oxo-hydroxo clusters of growing size from the literature (from the Ce-{6} to Ce-{38}). By doing so, we fill the gap between Ce molecular assemblies and the smaller nanometric CeO_2 NPs. The samples are characterized by single crystal XRD in order to validate a full atomic scale structure. The corresponding HEXS and HERFD-XAS measurements at the Ce L_{III} edge are then compared as a function of the particle size. The results show a continuous evolution of both the structural (HEXS) and electronic properties (HERFD) going from molecular compounds to large polynuclear assemblies that continues up to periodic cerium dioxides materials. In more detail, the PDF reveals a split of the Ce-O coordination shell for the smallest assemblies that are not present in the CeO_2 bulk. The analysis of the oxo-hydroxo clusters crystal structure shows that this change is due to the predominance of surface Ce atoms that coordinates in nine-fold distorted trigonal tricapped geometries while core atoms are in O_h like point group similar to the one of CeO_2. This structural trend translates very clearly to the samples electronic properties probed using high resolution Ce L_{III} edge with HERFD-XAS. Decreasing the particle size increases the ratio in the surface to/bulk atomic sites in the single crystal clusters resulting in a concomitant decrease of the e_g/t_{2g} splitting. While the CeO_2 L_{III} edge spectrum reveals a large split due to crystal field effect on Ce 5d orbitals, this split becomes lower in small NPs and molecular clusters. Overall, we report here for the first consistent set of HERFD experiments including a Ce^{4+} solution (stabilized under electro-chemical conditions) up to CeO_2. Moreover, the following Ce L_{III} edge simulations enable to understand the effect of surface to/bulk ratio on the spectral properties of individual samples. In polynuclear clusters, the calculations was applied for individual crystallographic sites showing how the e_g/t_{2g} splitting modeled for the core Ce atoms transforms into a single broad peak for the surface atoms similar to the one measured and modeled for hexanuclear clusters. The combination of these different sites HERFD signals, according to the respective Ce_{core}/Ce_{total} ratio, results in an accurate reproduction of experimental spectra. This approach was then extended for the simulation of Ce L_{III} spectra as a function of the Ce_{core}/Ce_{total} ratio and compared to the experimental CeO_2 NPs spectra using a Δ_{Oh} split as an empirical parameter. Both experimental measurements and

simulation converge to a relation between the size and Ce 5d orbital states. We suggest that, in future studies, this relation may be a useful to estimate particle size during in-situ measurements using HERFD-XAS at the Ce L_{III} edge.

AUTHOR INFORMATION

Corresponding author

*K. K.: phone. +33 4 76 88 23 67; e-mail. kristina.kvashnina@esrf.fr

*T. D.: phone. + 33 4 66 79 65 87; e-mail. thomas.dumas@cea.fr

ORCID

Paul Estevenon: 0000-0001-8517-4744

Lucia Amidani: 0000-0003-2234-4173

Stephen Bauters: 0000-0001-5484-8857

Christelle Tamain: 0000-0002-3492-6536

Christoph Hennig: 0000-0001-6393-2778

Thomas Dumas: 0000-0001-6425-6484

Kristina Kvashnina: 0000-0003-4447-4542

Notes

The authors declare no competing financial interest.

ACKNOWLEDGMENTS

REFERENCES

1. A. Trovarelli, *Catalysis Reviews*, 1996, **38**, 439-520.
2. E. Perry Murray, T. Tsai and S. A. Barnett, *Nature*, 1999, **400**, 649-651.
3. S. Sharma, S. Hilaire, J. M. Vohs, R. J. Gorte and H.-W. Jen, *Journal of Catalysis*, 2000, **190**, 199-204.
4. V. V. Kharton, F. M. FIgueiredo, L. Navarro, E. N. Naumovich, A. V. Kovalevsky, A. A. Yaremchenko, A. P. Viskup, A. Carneiro, F. M. B. Marques and J. R. Frade, *Journal of Materials Science*, 2001, **36**, 1105-1117.
5. Y. Xijuan, X. Pingbo and S. Qingde, *Physical Chemistry Chemical Physics*, 2001, **3**, 5266-5269.
6. X. Qi and M. Flytzani-Stephanopoulos, *Industrial & Engineering Chemistry Research*, 2004, **43**, 3055-3062.
7. V. K. Ivanov, A. B. Shcherbakov and A. V. Usatenko, *Russian Chemical Reviews*, 2009, **78**, 855-871.
8. V. K. Ivanov, O. S. Polezhaeva and Y. D. Tret'yakov, *Russian Journal of General Chemistry*, 2010, **80**, 604-617.
9. Q. Wang, B. Zhao, G. Li and R. Zhou, *Environmental Science and Technology*, 2010, **44**, 3870-3875.
10. H. Imagawa, A. Suda, K. Yamamura and S. Sun, *Journal of Physical Chemistry C*, 2011, **115**, 1740-1745.
11. I. Celardo, J. Z. Pedersen, E. Traversa and L. Ghibelli, *Nanoscale*, 2011, **3**, 1411-1420.
12. L. Jiang, M. Yao, B. Liu, Q. Li, R. Liu, H. Lv, S. Lu, C. Gong, B. Zou, T. Cui, B. Liu, G. Hu and T. Wågberg, *Journal of Physical Chemistry C*, 2012, **116**, 11741-11745.
13. N. M. Zholobak, V. K. Ivanov, A. B. Shcherbakov, A. S. Shaporev, O. S. Polezhaeva, A. Y. Baranchikov, N. Y. Spivak and Y. D. Tretyakov, *Journal of Photochemistry and Photobiology B: Biology*, 2011, **102**, 32-38.
14. C. Sun, H. Li and L. Chen, *Energy & Environmental Science*, 2012, **5**, 8475-8505.
15. S. P. S. Badwal, D. Fini, F. T. Ciacchi, C. Munnings, J. A. Kimpton and J. Drennan, *Journal of Materials Chemistry A*, 2013, **1**, 10768-10782.
16. L. Fan, C. Wang, M. Chen and B. Zhu, *Journal of Power Sources*, 2013, **234**, 154-174.
17. K. Anupriya, E. Vivek and B. Subramanian, *Journal of Alloys and Compounds*, 2014, **590**, 406-410.
18. K. Reed, A. Cormack, A. Kulkarni, M. Mayton, D. Sayle, F. Klaessig and B. Stadler, *Environmental Science: Nano*, 2014, **1**, 390-.
19. M. Shishkin and T. Ziegler, *Physical Chemistry Chemical Physics*, 2014, **16**, 1798-1808.
20. C. E. Castano, M. J. O'Keefe and W. G. Fahrenholtz, *Current Opinion in Solid State and Materials Science*, 2015, **19**, 69-76.
21. C.-N. Liu, M. Wiesener, I. Giner and G. Grundmeier, *Frontiers in Materials*, 2015, **2**, 68.

22. N. M. Zholobak, A. B. Shcherbakov, E. O. Vitukova, A. V. Yegorova, Y. V. Scripinets, I. I. Leonenko, A. Y. Baranchikov, A. P. and V. K. Ivanov, *RSC Advances*, 2014, **4**, 51703-51710.

23. M. Machida, T. Kawada, H. Fujii and S. Hinokuma, *Journal of Physical Chemistry C*, 2015, **119**, 24932-24941.

24. A. Sharma, M. Varshney, J. Jaehun Park, T. K. Ha, K. H. Chaeb and H. J. Shin, *Physical Chemistry Chemical Physics*, 2015, **17**, 30065-30075.

25. C. Walkey, S. Das, S. Seal, J. Erlichman, K. Heckman, L. Ghibelli, E. Traversa, J. F. McGinnis and W. T. Self, *Environmental Science: Nano*, 2015, **2**, 33-53.

26. X. Han, N. Amrane, Z. Zhang and M. Benkraouda, *Journal of Physical Chemistry C*, 2016, **120**, 13325−13331.

27. T. Montini, M. Melchionna, M. Monai and P. Fornasiero, *Chemical Reviews*, 2016, **116**, 5987-6041.

28. A. Dhall and W. Self, *Antioxidants*, 2018, **7**, 97.

29. P. Li, X. Chen, Y. Li and J. W. Schwank, *Catalysis Today*, 2019, **327**, 90-115.

30. Y. Ogura, K. Sato, S. I. Miyahara, Y. Kawano, T. Toriyama, T. Yamamoto, S. Matsumura, S. Hosokawa and K. Nagaoka, *Chemical Science*, 2018, **9**, 2230-2237

31. T. Jia, J. Xu, S. Dong, F. He, C. Zhong, G. Yang, H. Bi, M. Xu, Y. Hu, D. Yang, P. Yang and J. Lin, *Chemical Science*, 2019, **10**, 8618-8633

32. G. Gasperi, L. Amidani, F. Benedetti, F. Boscherini, P. Glatzel, S. Valeri and P. Luches, *Physical Chemistry Chemical Physics*, 2016, **18**, 20511-20517.

33. R. Schmitt, A. Nenning, O. Kraynis, R. Korobko, A. I. Frenkel, I. Lubomirsky, S. M. Hailef and J. L. M. Rupp, *Chemical Society Reviews*, 2020, **49**, 554-592.

34. H. S. Kim, C. Y. Joung, B. H. Lee, J. Y. Oh, Y. H. Koo and P. Heimgartner, *Journal of Nuclear Materials*, 2008, **378**, 98-104.

35. X. Beaudoux, M. Virot, T. Chave, G. Leturcq, G. Jouan, L. Venault, P. Moisy and S. I. Nikitenko, *Dalton Transactions*, 2016, **45**, 8802-8815.

36. D. Andreescu, G. Bulbul, R. E. Özel, A. Hayat, N. Sardesai and S. Andreescu, *Environmental Science: Nano*, 2014, **1**, 445-458

37. I. Römer, S. M. Briffa, Y. Arroyo Rojas Dasilva, D. Dimitri Hapiuk, V. Trouillet, R. E. Palmer and E. Valsami-Jones, *Plos One*, 2019, **14**, e0217483.

38. C. Artini, M. Pani, M. M. Carnasciali, M. T. Buscaglia, J. R. Plaisier and G. A. Costa, *Inorganic Chemistry*, 2015, **15**, 4126–4137.

39. T. V. Plakhova, A. Y. Romanchuk, S. M. Butorin, A. D. Konyukhova, A. V. Egorov, A. A. Shiryaev, A. E. Baranchikov, P. V. Dorovatovskii, T. Huthwelker, E. Gerber, S. Bauters, M. M. Sozarukova, A. C. Scheinost, V. K. Ivanov, S. N. Kalmykov and K. O. Kvashnina, *Nanoscale*, 2019, **11**, 18142-18149.

40. D. Prieur, W. Bonani, K. Popa, O. Walter, K. W. Kriegsman, M. H. Engelhard, X. Guo, R. Eloirdi, T. Gouder, A. Beck, T. Vitova, A. C. Scheinost, K. O. Kvashnina and P. Martin, *Inorganic Chemistry*, 2020, **59**, 5760-5767.

41. C. R. Martin, G. A. Leitha and N. B. Shustova, *Chemical Science*, 2021, **12**, 7214-7230

42. K. J. Mitchell, K. A. Abboud and G. Christou, *Nature Communications*, 2017, **8**, 1445.
43. A. Ikeda-Ohno, S. Tsushima, C. Hennig, T. Yaita and G. Bernhard, *Dalton Transactions*, 2012, **41**, 7190-7192.
44. T. J. Demars, M. K. Bera, S. Seifert, M. R. Antonio and R. J. Ellis, *Angewandte Chemie - International Edition*, 2015, **54**, 7644-7648.
45. N. Guillou, J. P. Auffrédic and D. Louër, *Journal of Solid State Chemistry*, 1994, **112**, 45-52.
46. S. Duval, X. Trivelli, P. Roussel and T. Loiseau, *European Journal of Inorganic Chemistry*, 2016, 5373–5379.
47. M. Dufaye, S. Duval, K. Nursiah, G. Stoclet, X. Trivellic and T. Loiseau, *CrystEngComm*, 2018, **20**, 7144-7155.
48. S. Duval, S. Béghin, C. Falaise, X. Trivelli, P. Rabu and T. Loiseau, *Inorganic Chemistry*, 2015, **54**, 8271-8280.
49. G. Lundgren, *Recueil des Travaux Chimiques des Pays-Bas*, 1956, **75**, 585-588.
50. P. Toledano, F. Ribot and C. Sanchez, *Comptes rendu de l'Académie des Sciences*, 1990, **311**, 1315-1320.
51. V. Mereacre, A. M. Ako, M. N. Akhtar, A. Lindemann, C. E. Anson and A. K. Powell, *Helvetica Chimica Acta*, 2009, **92**, 2507-2524.
52. C. Hennig, A. Ikeda-Ohno, W. Kraus, S. Weiss, P. Pattison, H. Emerich, P. M. Abdala and A. C. Scheinost, *Inorganic Chemistry*, 2013, **52**, 11734-11743.
53. L. Mathey, M. Paul, C. Copéret, H. Tsurugi and K. Mashima, *Chemistry - A European Journal*, 2015, **21**, 13454-13461.
54. S. L. Estes, M. R. Antonio and L. Soderholm, *Journal of Physical Chemistry C*, 2016, **120**, 5810-5818.
55. S. Matsunaga, Y. Inoue, K. Mihara and K. Nomiya, *Inorganic Chemistry Communications*, 2017, **80**, 61-64.
56. M. Dufaye, S. Duval, G. Stoclet and T. Loiseau, *CrystEngComm*, 2020, **22**, 371–380.
57. R. Das, R. Sarma and J. B. Baruah, *Inorganic Chemistry Communications*, 2010, **13**, 793-795.
58. I. L. Malaestean, A. Ellern, S. Baca and P. Kögerler, *Chemical Communications*, 2012, **48**, 1499-1501.
59. S. Duval, P. Roussel and T. Loiseau, *Inorganic Chemistry Communications*, 2017, **83**, 52–54.
60. M. C. Wasson, X. Zhang, K.-I. Otake, A. S. Rosen, S. Alayoglu, M. D. Krzyaniak, Z. Chen, L. R. Redfern, L. Robison, F. A. Son, Y. Chen, T. Islamoglu, J. M. Notestein, R. Q. Snurr, M. R. Wasielewski and O. K. Farha, *Chemistry of Materials*, 2020, **32**, 8522-8529.
61. R. Husar, T. Dumas, M. L. Schlegel, D. Schlegel, D. Guillaumont, P. L. Solari and P. Moisy, *Journal of Synchrotron Radiation*, 2022, **29**, 1-10.
62. D. Bengio, T. Dumas, S. Arpigny, R. Husar, E. Mendes, P. L. Solari, M. L. Schlegel, D. Schlegel, S. Pellet-Rostaing and P. Prof. Philippe Moisy, *Chemistry - A European Journal*, 2020, **26**, 14385-14396.

63. A. C. Scheinost, J. Claussner, J. Exner, M. Feig, S. Findeisen, C. Hennig, K. O. Kvashnina, D. Naudet, D. Prieur, A. Rossberg, M. Schmidt, C. Qiu, P. Colomp, C. Cohen, E. Dettona, V. Dyadkin and T. Stumpf, *Journal of Synchrotron Radiation*, 2021, **28**, 333-349.

64. V. Dyadkin, P. Pattison, V. Dmitriev and D. Chernyshov, *Journal of Synchrotron Radiation*, 2016, **23**, 825-829.

65. J. Kieffer and J. P. Wright, *Powder Diffr*, 2013, **28**, S339-S350.

66. K. O. Kvashnina and A. C. Scheinost, *Journal of Synchrotron Radiation*, 2016, **23**, 836-841.

67. G. B. M. Vaughan, R. Baker, R. Barret, J. Bonnefoy, T. Buslaps, S. Checchia, D. Duran, F. Fihman, P. Got, J. Kieffer, S. A. J. Kimber, K. Martel, C. Morawe, D. Mottin, E. Papillon, S. Petitdemange, A. Vamvakeros, J. P. Vieux and M. Di Michiel, *Journal of Synchrotron Radiation*, 2020, **27**, 515–528.

68. J. Kieffer, S. Petitdemange and T. Vincent, *Journal of Synchrotron Radiation*, 2018, **25**, 612–617.

69. T. D. P. Juhás, C. L. Farrow, S. J. L. Billinge, *Journal of Applied Crystallography*, 2013, **46**, 560–566.

70. L. B. Skinner, C. J. Benmore and J. B. Parise, *Nuclear Instruments and Methods in Physics Research Section A: Accelerators, Spectrometers, Detectors and Associated Equipment*, 2012, **662**, 61-70.

71. P. Juhás, C. L. Farrow, X. Yang, K. R. Knox and S. J. L. Billinge, *Acta Crystallographica Section A*, 2015, **71**, 562–568.

72. J. J. Rehr, J. J. Kas, F. D. Vila, M. P. Prange and K. Jorissen, *Physical Chemistry Chemical Physics*, 2010, **12**, 5503-5513.

73. Y. Li, O. Kraynis, J. Kas, T. C. Weng, D. Sokaras, R. Zacharowicz, I. Lubomirsky and A. I. Frenkel, *AIP Advances*, 2016, **6**, 055320.

74. S. J. L. Billinge and I. Levin, *Science*, 2007, **316**, 561–565.

75. B. Gilbert, F. Huang, H. Zhang, G. A. Waychunas and J. F. Banfield, *Science*, 2004, **305**, 651–654.

76. K. M. Ø. Jensen, A. B. Blichfeld, S. R. Bauers, S. R. Wood, E. Dooryhée, D. C. Johnson, B. B. Iversen and S. J. L. Billinge, *IUCrJ*, 2015, **2**, 481–489.

77. S. Takao, K. Takao, W. Kraus, F. Emmerling, A. C. Scheinost, G. Bernhard and C. Hennig, *European Journal of Inorganic Chemistry*, 2009, 4771-4775.

78. C. Tamain, T. Dumas, C. Hennig and P. Guilbaud, *Chemistry - A European Journal*, 2017, **10**, 1002.

79. L. Bonato, M. Virot, T. Dumas, A. Mesbah, E. Dalodière, O. Dieste Blanco, T. Wiss, X. Le Goff, M. Odorico, D. Prieur, A. Rossberg, L. Venault, N. Dacheux, P. Moisy and S. I. Nikitenko, *Nanoscale Advances*, 2020, **2**, 214-224.

80. K. O. Kvashnina, S. M. Butorin and P. Glatzel, *Journal of Analytical Atomic Spectrometry*, 2011, **26**, 1265-1272.

81. A. Kotani, K. O. Kvashnina, S. M. Butorin and P. P. Glatzel, *The European Physical Journal B*, 2012, **85**, 257.

82. A. Kotani, K. O. Kvashnina, S. M. Butorin and P. Glatzel, *Journal of Electron Spectroscopy and Related Phenomena*, 2011, **184**, 210-215.

83. A. Bianconi, A. Marcelli, H. Dexpert, R. Karnatak, A. Kotani, T. Jo and J. Petiau, *Physical Reviews B*, 1987, **35**, 806-812.

84. A. V. Soldatov, T. S. Ivanchenko, A. Kotani and A. Bianconi, *Physica B: Condensed Matter*, 1995, **20/-209**, 53-55.

85. C. Paun, O. V. Safonova, J. Szlachetko, P. M. Abdala, M. Nachtegaal, J. Sa, E. Kleymenov, A. Cervellino, F. Krumeich and J. A. van Bokhoven, *Journal of Physical Chemistry C*, 2012, **116**, 7312-7317.

From molecular oxo-hydroxo Ce clusters to crystalline CeO_2

Paul Estevenon[1,2,3], Lucia Amidani,[1,2] Stephen Bauters,[1,2] Christelle Tamain,[3] Michael Bodensteiner,[4] Florian Meuer,[4] Christoph Hennig,[1,2] Thomas Dumas,[3,*] Kristina Kvashnina[1,2,*]

[1] Helmholtz Zentrum Dresden Rossendorf (HZDR), Institute of Resource Ecology, 01314 Dresden, Germany.

[2] The Rossendorf Beamline at ESRF−The European Synchrotron, 38043 Grenoble, Cedex 9, France.

[3] CEA, DES, ISEC, DMRC, Univ Montpellier, Marcoule, France.

[4] Universität Regensburg, Fakultät für Chemie und Pharmazie, Universitätsstr. 31, 93053 Regensburg, Germany

SUPPORTING INFORMATION

Sample preparation:

$[Ce_6(\mu_3\text{-}O)_4(\mu_3\text{-}OH)_4(NH_3CH_2COO)_8(NO_3)_4(H_2O)_6]Cl_8 \cdot 8H_2O$ (**Ce-{6}-SI-1**) has been prepared according to the protocol described by Estes et al. [1] by dissolving 0.750 g of $(NH_4)_2Ce(NO_3)_6$ ($(NH_4)_2Ce(NO_3)_6$, Sigma Aldrich ≥ 98%) (1.4 mmol) and 0.150 g of glycine (NH_2CH_2COOH, Sigma Aldrich ≥ 99%) (2.0 mmol) in 0.9 mL of water (50.0 mmol) in a glass vial. A saturated NaCl (LaboSI ≥ 99.8%) aqueous solution, ≈ 6.1 $mol \cdot L^{-1}$, was prepared alongside. 5.35 g (≈ 4.45 mL) of that solution were added to the first one (NaCl 27.1 mmol; H_2O 209 mmol). The vial was left open allowing a slow evaporation and maintained undisturbed a few days leading to the cluster crystallization.

$[Ce_6(\mu_3\text{-}O)_4(\mu_3\text{-}OH)_4(NH_3CH_2COO)_9(NO_3)_5H_2O](NO_3)_7 \cdot 6{-}7H_2O$ (**Ce-{6}-SI-2**) has been prepared according to the protocol described by Estes et al. [1] by dissolving 0.820 g of $(NH_4)_2Ce(NO_3)_6$ (1.5 mmol) and 0.365 g of glycine (4.9 mmol) in 0.5 mL of a 10^{-2} $mol \cdot L^{-1}$ NaOH (NaOH, Sigma Aldrich ≥ 97%) aqueous solution (H_2O 27.8 mmol; NaOH 5 µmol) in a glass vial. Then, 15 µL of concentrated HNO_3 (HNO_3 65%, VWR) (H_2O 0.8 mmol; HNO_3 0.2 mmol) was added to the reactive media. Finally, the solution was maintained undisturbed for a few days leading to the cluster crystallization.

$[Ce_6(\mu_3\text{-}O)_4(\mu_3\text{-}OH)_4(HCOO)_{10}(NO_3)_4] \cdot (NO_3)_3(NH_4)_5(H_2O)_5$ (**Ce-{6}-SI-3**) has been prepared according to the protocol described by Hennig et al. [2]. An aqueous solution was prepared by mixing 0.548 g of $(NH_4)_2Ce(NO_3)_6$ (1.0 mmol), 0.386 mL of formic acid (HCOOH, Fluka ≥ 98%) (10 mmol), 71.5 µL of concentrated HNO_3 (HNO_3 65%, VWR) (HNO_3: 1 mmol; H_2O: 2 mmol) and 0.55 mL of water (31 mmol). The pH of the reactive media was adjusted around 0.2 by addition of NaOH 8 $mol \cdot L^{-1}$ then the solution was centrifuged 10 min at 3,500 rpm, the supernatant was put in a glass vial which was left open allowing a slow evaporation and maintained undisturbed several days.

$[Ce_{40}O_{56}(OH)_2(CH_3CO_2)_{44}(CH_3CN)_2(C_5H_5N)_4] \cdot 48CH_3CN$ (**Ce-{40}**) has been prepared according to the protocol described by Mitchell et al. [3]. A mixture of 1 mL of pyridine (C_5H_5N, Prolabo ≥ 99.8%) (12.4 mmol), 100 µL of water (5.6 mmol) and 23 µL of propionic acid (CH_3CO_2H, Prolabo ≥ 99%) (0.4 mmol) was prepared and added on 0.055 g of $(NH_4)_2Ce(NO_3)_6$ (0.1 mmol) and 0.015 g of ammonium iodide (NH_4I, Acros Orga ≥ 98%) (0.1 mmol). The mixture obtained was stirred at 500 rpm during 30 min. Then 2 mL of

acetonitrile (CH_3CN, Sigma Aldrich ≥ 99.8%) (38.3 mmol) has been added on this mixture and the solution was maintained undisturbed for several weeks leading to the formation of crystals.

Crystal structure:

Table S1. Crystal data and structure refinement parameters for Ce-{38} and Ce-{24}.

	Ce-{38}	**Ce-{24}**
Formula	$C_{149.25}H_{220}Ce_{38}N_{8.25}O_{134}$	$C_{127.5}H_{172.5}Ce_{24}N_{7.5}O_{94}$
$D_{calc.}$/ g cm^{-3}	2.600	2.288
m/mm^{-1}	4.826	3.868
Formula Weight	9598.38	6677.10
Colour	clear colourless	clear brown
Shape	platelet-shaped	block-shaped
Size/mm^3	0.18×0.18×0.14	0.07×0.06×0.06
T/K	108.37	100
Crystal System	monoclinic	monoclinic
Space Group	$C2/m$	$P2_1/n$
a/Å	29.13640(10)	20.56554(17)
b/Å	28.13810(10)	19.84585(19)
c/Å	29.93190(10)	23.7424(3)
a/°	90	90
b/°	92.26	90.1615(9)
g/°	90	90
V/Å^3	24520.30(15)	9690.19(17)
Z	4	2
Z'	0.5	0.5
Wavelength/Å	0.61862	0.61862
Radiation type	Synchrotron	Synchrotron
Q_{min}/°	1.493	1.447
Q_{max}/°	24.357	20.101
Measured Refl's.	268096	136503
Indep't Refl's	30465	13902
Refl's I≥2 s(I)	24648	9370
R_{int}	0.1003	0.0877
Parameters	1864	1242
Restraints	1186	1200
Largest Peak	2.683	3.350
Deepest Hole	-1.603	-0.845
GooF	1.126	1.055
wR_2 (all data)	0.1096	0.2705
wR_2	0.1061	0.2432
R_1 (all data)	0.0409	0.1055
R_1	0.0351	0.0822

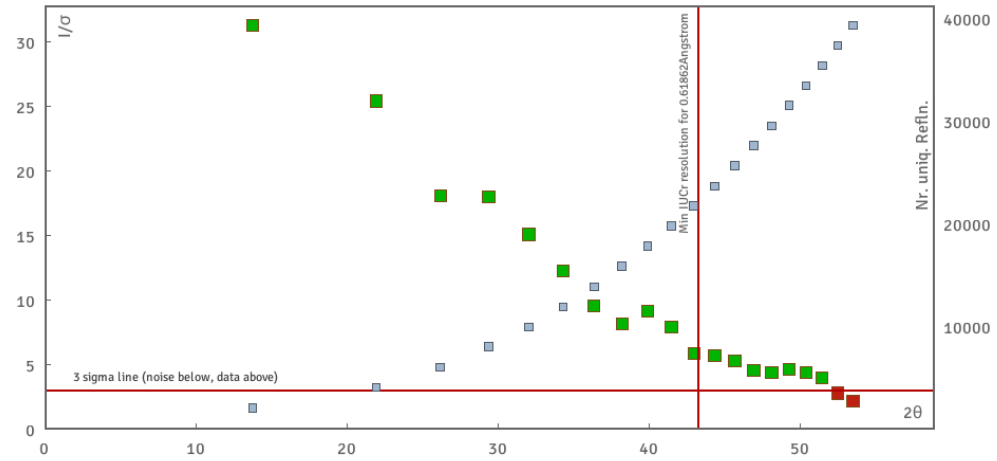

Figure S1. I/σ vs. resolution for **Ce-{38}**.

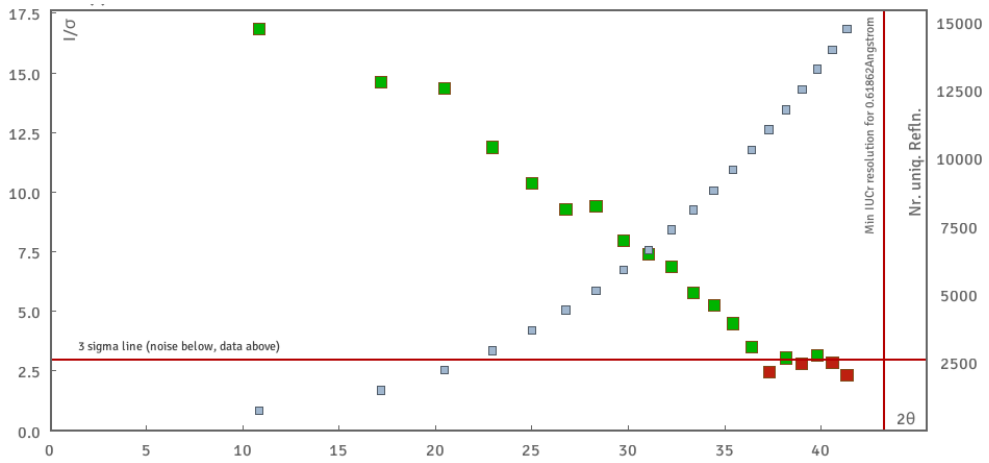

Figure S2. I/σ vs. resolution for **Ce-{24}**. The scattering is weak despite synchrotron radiation. This limits the resolution.

Table S2. Coordination number (CN) Bond Valence Sums for Ce^{3+} and Ce^{4+} in Ce-{38}.

Ce-{38} a			
Atom	CN	Ce^{3+}	Ce^{4+}
Ce01	9	4.42	**3.92**
Ce02	9	4.32	**3.83**
Ce03	9	3.62	**3.80**
Ce04	9	4.32	**3.83**
Ce05	8	4.56	**3.96**
Ce06	9	4.42	**4.22**
Ce07	8	4.57	**3.83**
Ce08	8	4.70	**4.13**
Ce09	8	4.58	**3.98**
Ce10	8	4.64	**4.08**
Ce11	9	4.66	**4.14**

Ce-{38} b			
Atom	CN	Ce^{3+}	Ce^{4+}
Ce12	9	4.20	**3.74**
Ce13	9	4.30	**3.82**
Ce14	8	4.66	**4.10**
Ce15	8	4.67	**4.11**
Ce16	9	4.43	**3.92**
Ce17	9	4.41	**3.90**
Ce18	9	4.41	**3.90**
Ce19	8	4.55	**3.96**
Ce20	9	4.46	**3.95**
Ce21	8	4.64	**4.08**
Ce22	8	4.51	**3.93**
Ce23	9	4.35	**3.89**
Ce24	9	4.38	**3.87**

Table S3. Coordination number (CN) Bond valence Sums for Ce^{3+} and Ce^{4+} in Ce-{24}.

Ce-{24}			
Atom	CN	Ce^{3+}	Ce^{4+}
Ce01	8	4.69	**4.13**
Ce02	8	4.40	**3.88**
Ce03	8	4.32	**3.81**
Ce04	9	4.30	**4.07**
Ce05	8	4.04	**3.57**
Ce06	9	4.40	**3.90**
Ce07	8	4.07	**3.59**
Ce08	10	**3.11**	2.83
Ce09	8	4.17	**3.68**
Ce10	9	4.45	**3.94**
Ce11	8	4.04	**3.57**
Ce12	9	4.39	**3.89**

Table S4. Bond Valence Sums and Assignment for O Atoms in Ce-{24}.

Ce-{24}		
Atom	BVS	Assignment
O1A	2.11	O^{2-}
O2A	2.04	O^{2-}
O3A	0.75	μ_4-OH^-
O4A	2.15	O^{2-}
O5A	1.71	O^{2-}
O7A	1.93	O^{2-}
O8A	1.93	O^{2-}
O9A[a]	1.23	μ_3-OH^-
O10A	2.09	O^{2-}
O11A	1.93	O^{2-}
O12A	1.95	O^{2-}
O14A	2.15	O^{2-}
O15A	1.68	O^{2-}
O16A	2.14	O^{2-}
O17A	2.00	O^{2-}
O18A	2.15	O^{2-}
O19A [a]	1.54	μ_3-OH^-
O20A	0.74	μ_4-OH^-

The bond valence was estimated following the equation of Brown and Aldermatt [4]

$$V_i = \sum s_{ij} = \sum exp\left[R_0 - r_{ij}/b\right]$$

Where V_i is the oxidation state of atom i, s_{ij} and r_{ij} are the valence and the bond length between atoms i and j, respectively. R_0 is the empirical determined distance typical for a given cation-anion pair, and b is a specific parameter. V equals the sum of all valences s_{ij} of a

coordination sphere around a metal ion. Its value approximates the formal oxidation state. The following values from Gagné and Hawthorne [5] and Trzeowska [6] were used. R_0 of Ce(III)-N was extrapolated.

Ce(III)-O : R_0 = 2.144 Å b = 0.389

Ce(IV)-O : R_0 = 2.046 Å b = 0.416

Ce(III)-N : R_0 = 2.277 Å b = 0.37

Ce(IV)-N : R_0 = 2.179 Å b = 0.37

Determination of the peak maxima and shoulder position:

The position of the B_1, B_2, C_1 and C_2 peaks (respectively B and C peaks for aqueous Ce(IV) in nitric acid and Ce-{6}) gathered in Table S5. were determined based on the first derivative of the HERFD spectra. In order to calculate the derivative, the spectra were smoothed by the Stavitzky-Golay method with windows of 5 points and second-degree polynomials. Then the smoothed curves were derived, the spectra local maxima were determined when the first derivative value decrease and its values is equal to zero (Figure S3). The position of the shoulders (B_1 and C_2 peaks for Ce-{24}, Ce-{38}, Ce-{40} and 2 nm CeO_2 samples) were determined from the first derivative, for B_1 peak when it reach it last local minima before the B_2 peak and for C_2 peak when it reach it first local maxima after the C_1 peak.

Table S5. Energy of the A, B_1, B_2, C_1 and C_2 peaks for the Ce(IV) in nitric media, the Ce-{6}, Ce-{24}, Ce-{38}, Ce-{40} clusters, CeO_2 NPs and bulk CeO_2.

	E_A (eV)	E_{B1} (eV)	E_{B2} (eV)	E_{C1} (eV)	E_{C2} (eV)
Ce^{4+}	5718.0	5726.6		5737.0	
Ce-{6}	5717.8	5726.6		5737.0	
Ce-{6}-SI-1	5717.8	5726.6		5737.0	
Ce-{6}-SI-2	5717.8	5726.6		5737.0	
Ce-{6}-SI-3	5718.0	5726.6		5737.0	
Ce-{24}	5717.8	5725.8	5727.2	5736.6	5737.6
Ce-{38}	5717.8	5725.2	5727.0	5736.6	5738.1
Ce-{40}	5717.6	5724.7	5727.4	5736.4	5738.0
CeO_2 NPs 2nm	5717.6	5725.0	5728.1	5736.2	5737.8
CeO_2 NPs 8nm	5717.8	5724.5	5728.4	5735.9	5738.4
Bulk CeO_2	5717.6	5724.3	5728.4	5735.9	5738.6
Simulated Ce-{38}	-	5724.9	5726.7	-	-
Simulated CeO_2	-	5724.1	5728.5	-	-

Table S6. Difference of energy observed for the splitting of the peaks corresponding of the electron transition from $2p_{3/2}$ to $5d_{5/2}$ states and Ce_{core}/Ce_{total} ratio considering a 2.3 Å surface layer.

	$\Delta_{Oh} = E_{B2} - E_{B1}$ (eV)	$E_{C2} - E_{C1}$ (eV)	Ce_{core}/Ce_{total} ratio
Ce^{4+}	0.0	0.0	0
Ce-{6}	0.0	0.0	0
Ce-{24}	1.4 ± 0.4	1.0 ± 0.4	0.25
Ce-{38}	1.8 ± 0.4	1.5 ± 0.4	0.37
CeO_2 NPs 2nm	3.1 ± 0.4	1.6 ± 0.4	0.46 ± 0.12
CeO_2 NPs 8nm	3.9 ± 0.4	2.5 ± 0.4	0.84 ± 0.05
Bulk CeO_2	4.1 ± 0.4	2.7 ± 0.4	1.00
Simulated Ce-{38}	1.8	-	0.37
Simulated CeO_2	4.5	-	1.00

Table S7. Δ_{Oh} factor calculated for CeO_2 NPs depending on the Ce_{core}/Ce_{total} ratio and corresponding particle size, considering a 2.3 Å surface layer..

Ce_{core}/Ce_{total} ratio	Δ_{Oh}	CeO_2 NPs size (nm)	Ce_{core}/Ce_{total} ratio	Δ_{Oh}	CeO_2 NPs size (nm)
0	0.60	-	0.43	3.19	1.9
0.05	0.79	0.7	0.44	3.24	1.9
0.1	1.03	0.9	0.45	3.28	2.0
0.15	1.21	1.0	0.5	3.46	2.3
0.2	1.37	1.1	0.55	3.58	2.5
0.25	1.55	1.2	0.6	3.69	2.9
0.3	1.73	1.4	0.65	3.78	3.4
0.35	1.93	1.6	0.7	3.86	4.1
0.36	1.98	1.6	0.75	3.93	5.0
0.37	2.04	1.6	0.8	4.00	6.4
0.38	2.12	1.7	0.85	4.05	8.7
0.39	2.21	1.7	0.9	4.11	13.3
0.4	2.33	1.7	0.95	4.15	27.2
0.41	2.61	1.8	1	4.20	core
0.42	3.08	1.8			

Table S8. Crystal structure of the cerium clusters.

	Ce-{6} [1]	**Ce-{6}-SI-1 [1]**	**Ce-{6}-SI-2 [1]**	**Ce-{6}-SI-3 [2]**
Formula	$C_{18}Ce_6N_{15}O_{44}$	$C_{16}H_{60}Ce_6Cl_8N_{12}O_{50}$	$C_{18}Ce_6N_{14}O_{42}$	$C_{10}H_{44}Ce_6N_{12}O_{54}$
MW (g·mol^{-1})	1971.05	2345.08	1925.04	2007.05
T (K)	100	100	100	296
λ (Å)	0.71073	0.71073	0.71073	0.71073
Crystallographic system	triclinic	tetragonal	triclinic	orthorhombic
Space group	$P\bar{1}$	$I4_1/a$	$P\bar{1}$	Pbcn
***a* (Å)**	15.0184(6)	22.3447(9)	15.5637(7)	12.3752(17)
***b* (Å)**	17.2016(7)	22.3447(9)	17.4963(8)	26.152(3)
***c* (Å)**	19.4927(8)	13.9211(6)	17.8639(8)	15.698(3)
α (°)	87.3718(6)	90	105.1843(7)	90
β (°)	79.5541(6)	90	99.5275(7)	90
γ (°)	66.3965(6)	90	105.1615(7)	90
V (Å^3)	4536.0(3)	6950.6(6)	4385.9(3)	5080.4(13)
Z	2	4	2	4

Table S8. (continuation).

	Ce-{24}	**Ce-{38}**	**Ce-{40} [3]**
Formula	$C_{127.5}H_{172.5}Ce_{24}N_{7.5}O_{94}$	$C_{149.25}H_{220}Ce_{38}N_{8.25}O_{134}$	$C_{112}H_{161}Ce_{40}N_5O_{148}$
MW (g·mol^{-1})	6677.10	9598.38	9550.20
T (K)	100	108.37	100
λ (Å)	0.61862	0.61862	0.71073
Crystallographic system	monoclinic	monoclinic	monoclinic
Space group	*P*2$_1$/*n*	*C*2/*m*	P2/m
***a* (Å)**	20.56554(17)	29.13640(10)	17.4795(7)
***b* (Å)**	19.84585(19)	28.13810(10)	21.0019(9)
***c* (Å)**	23.7424(3)	29.93190(10)	38.6269(16)
α (°)	90	90	90
β (°)	90.1615(9)	92.26	98.254(1)
γ (°)	90	90	90
V (Å^3)	9690.19(17)	24520.30(15)	14033.2(10)
Z	2	4	1

(a)

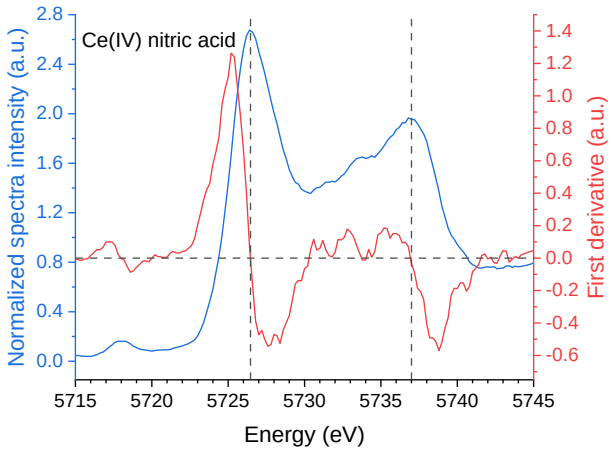
Ce(IV) nitric acid
Normalized spectra intensity (a.u.)
First derivative (a.u.)
Energy (eV)

(b)

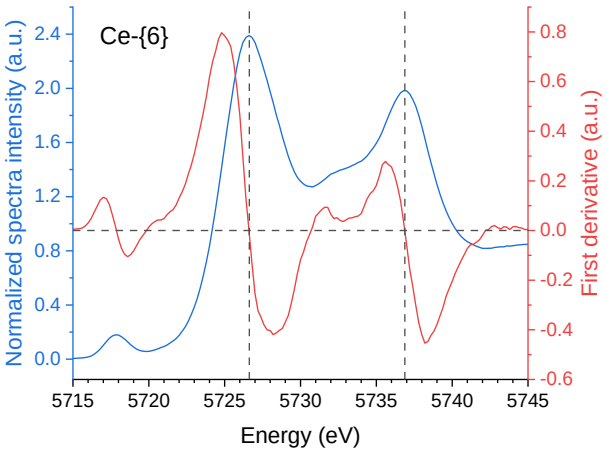
Ce-{6}
Normalized spectra intensity (a.u.)
First derivative (a.u.)
Energy (eV)

(c)

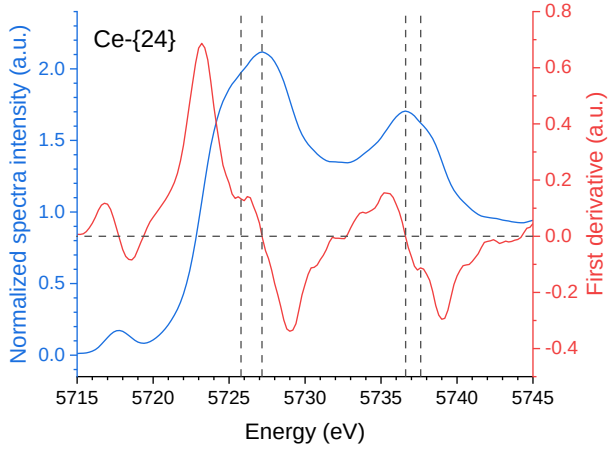
Ce-{24}
Normalized spectra intensity (a.u.)
First derivative (a.u.)
Energy (eV)

(d)

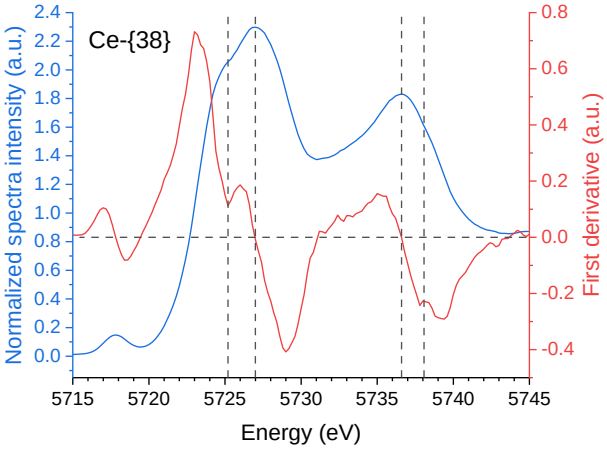
Ce-{38}
Normalized spectra intensity (a.u.)
First derivative (a.u.)
Energy (eV)

(e)

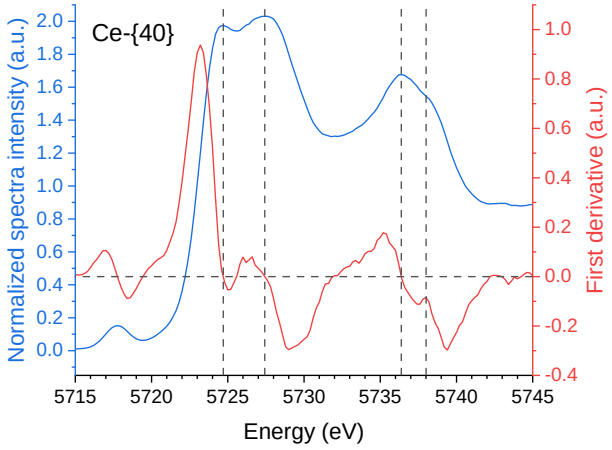
Ce-{40}
Normalized spectra intensity (a.u.)
First derivative (a.u.)
Energy (eV)

(f)

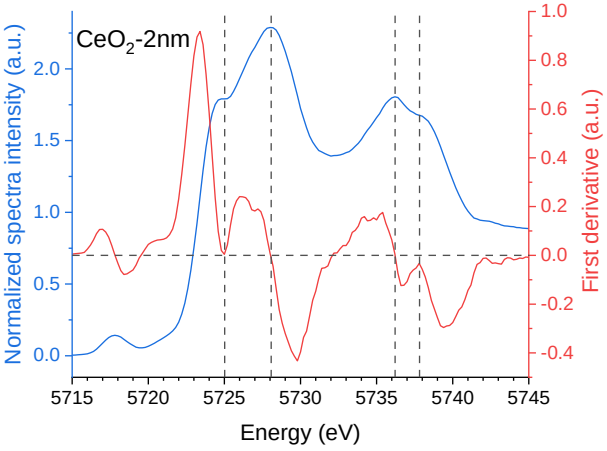
CeO2-2nm
Normalized spectra intensity (a.u.)
First derivative (a.u.)
Energy (eV)

(g)

(h)

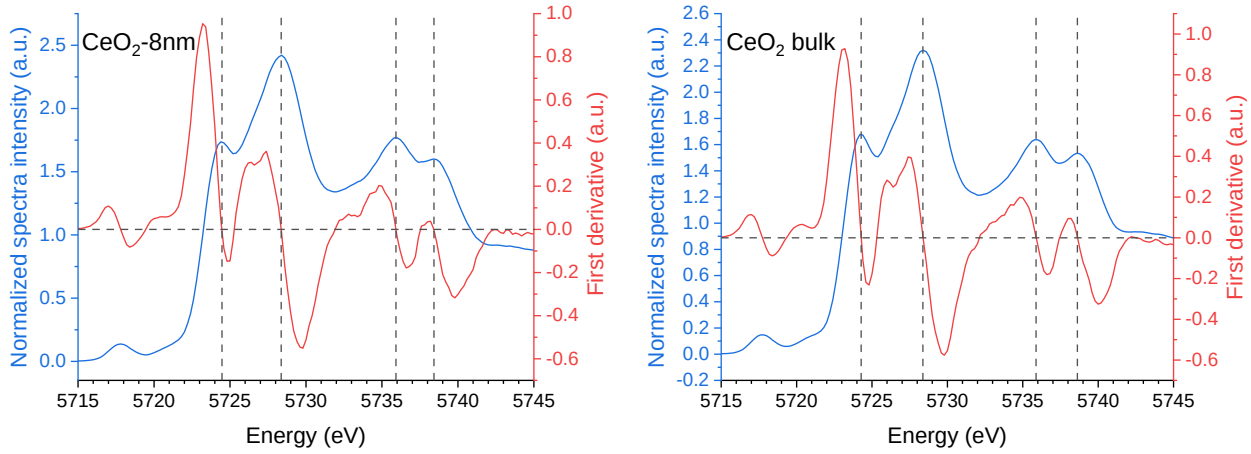

Figure S3. Smoothed HERFD spectra and its first derivative for Ce(IV) in nitric acid (a), Ce-{6} (b), Ce-{24} (c), Ce-{38} (d), Ce-{40} (e), CeO_2 NPs 2nm (f), CeO_2 NPs 2nm (g) and bulk CeO_2 (h).

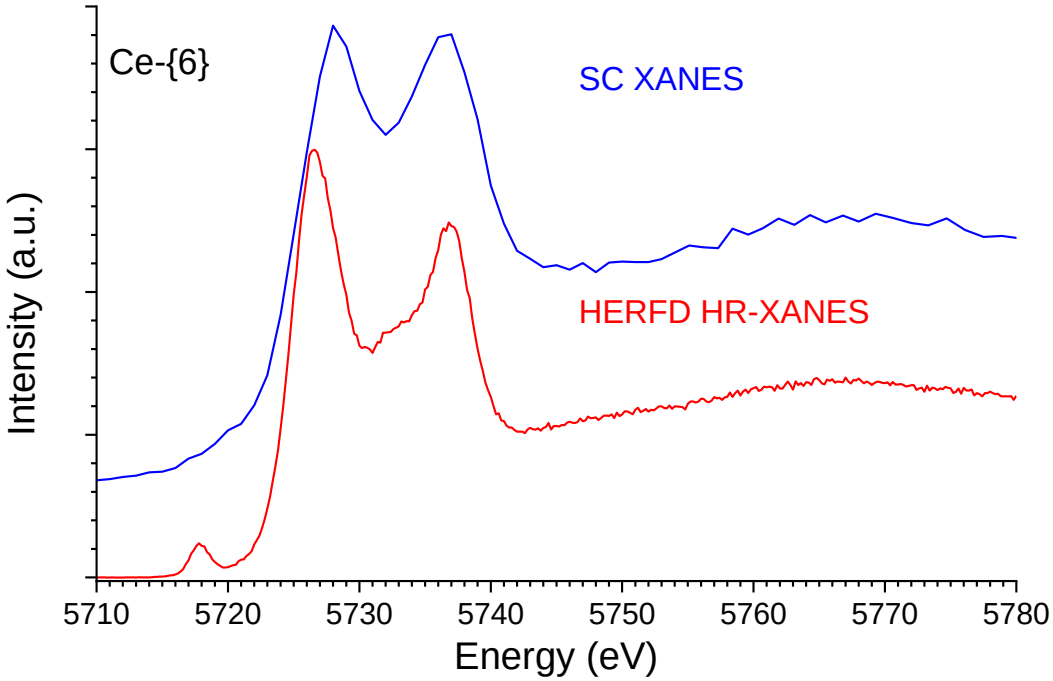

Figure S4. HERFD (a) and XANES on a single crystal sample (b) for Ce-{6} cluster at Ce L_{III} edge.

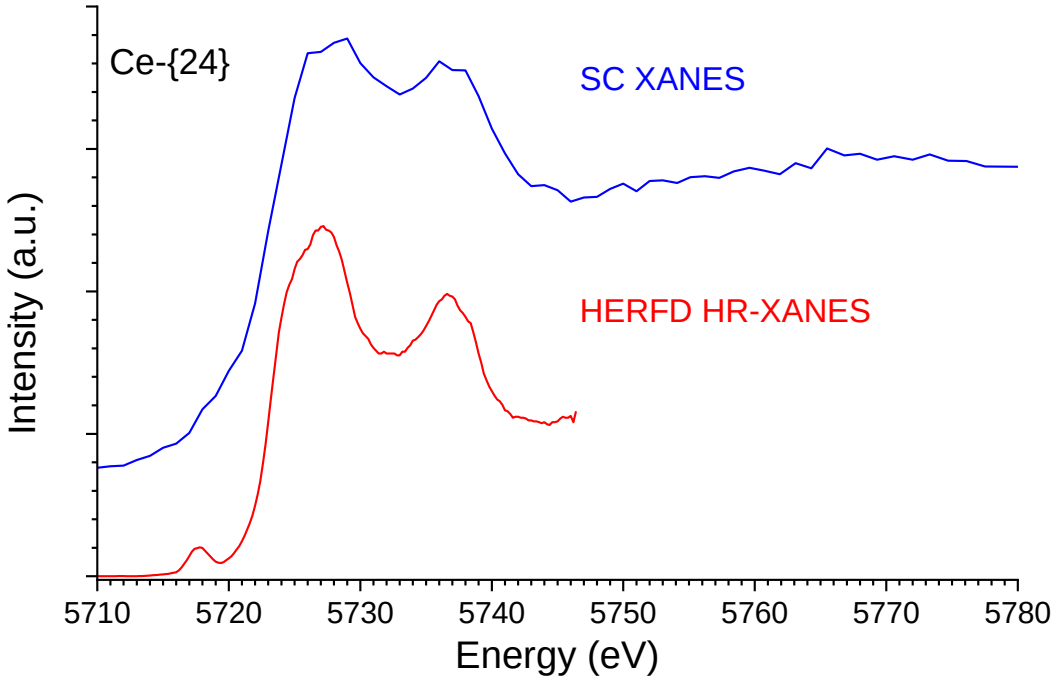

Figure S5. HERFD (a) and XANES on a single crystal sample (b) for Ce-{24} cluster at Ce L_{III} edge.

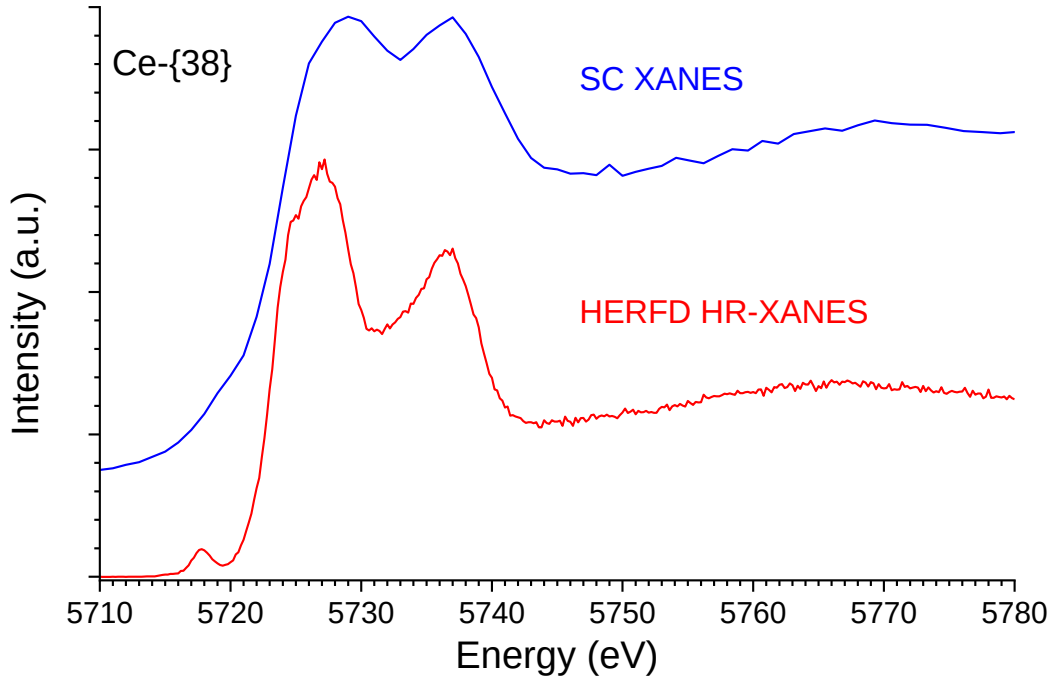

Figure S6. HERFD (a) and XANES on a single crystal sample (b) for Ce-{38} cluster at Ce L_{III} edge.

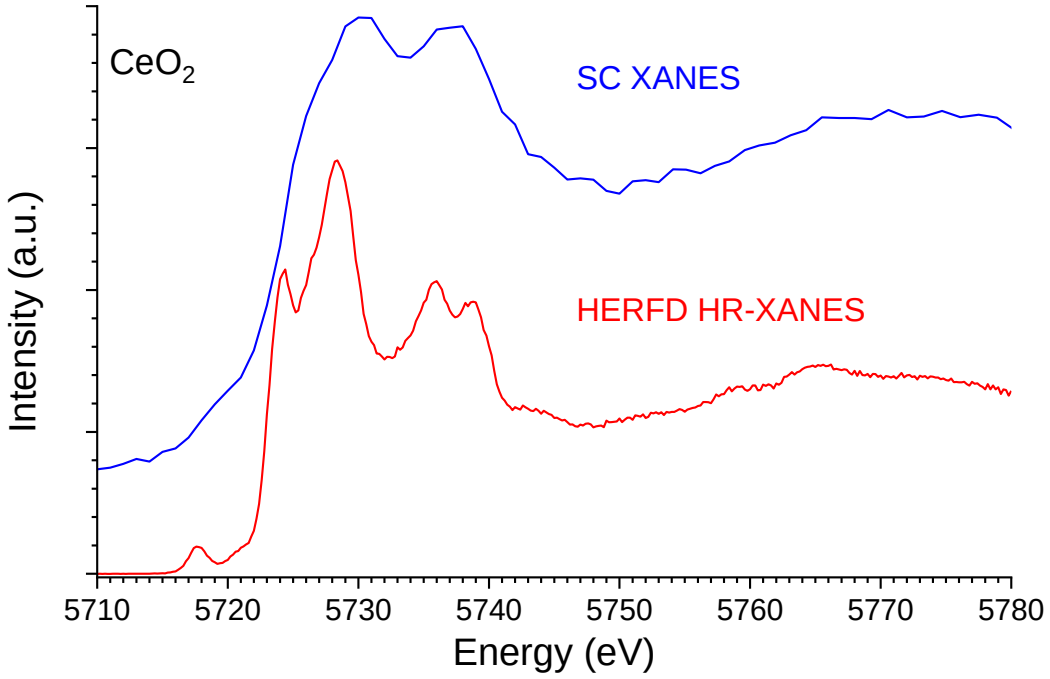

Figure S7. HERFD (a) and XANES on a single crystal sample (b) for bulk CeO_2 at Ce L_{III} edge.

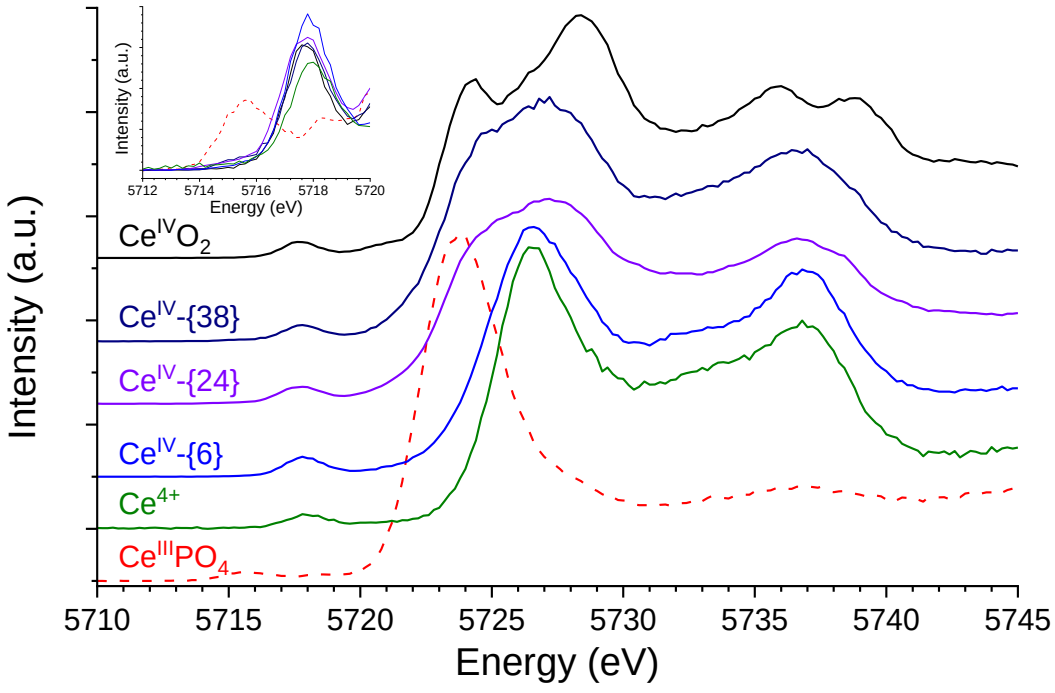

Figure S8. HERFD spectra at Ce L_{III} edge for aqueous Ce^{4+}, Ce-{6}, Ce-{24}, Ce-{38} and bulk CeO_2 samples compared to $CePO_4$.

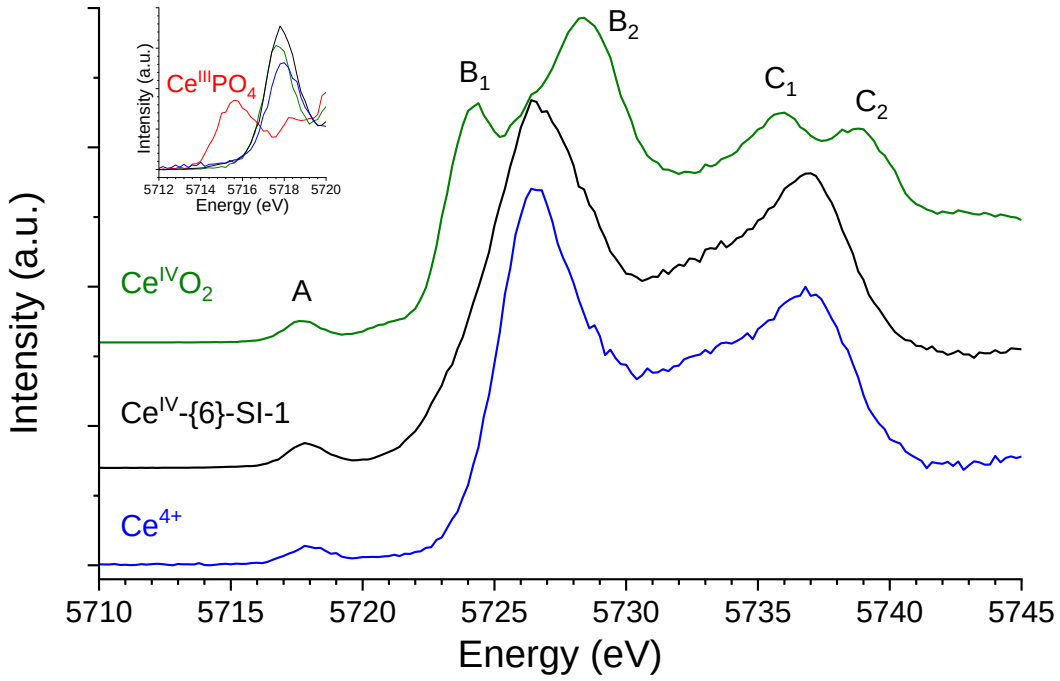

Figure S9. HERFD spectra at Ce L_{III} edge for the Ce-{6}-SI-1 clusters compared to aqueous Ce^{4+} and bulk CeO_2 references. The magnification of the pre-edge was reported in the inserts and compared to monazite as Ce(III) oxidation state reference.

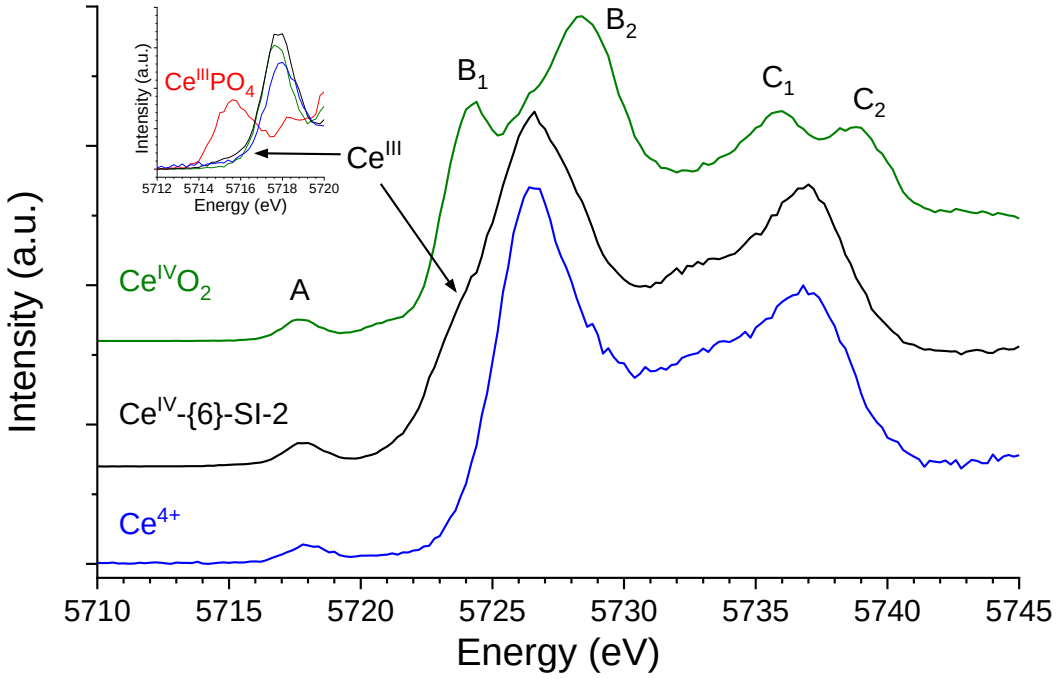

Figure S10. HERFD spectra at Ce L_{III} edge for the Ce-{6}-SI-2 clusters compared to aqueous Ce^{4+} and bulk CeO_2 references. The magnification of the pre-edge was reported in the inserts and compared to monazite as Ce(III) oxidation state reference.

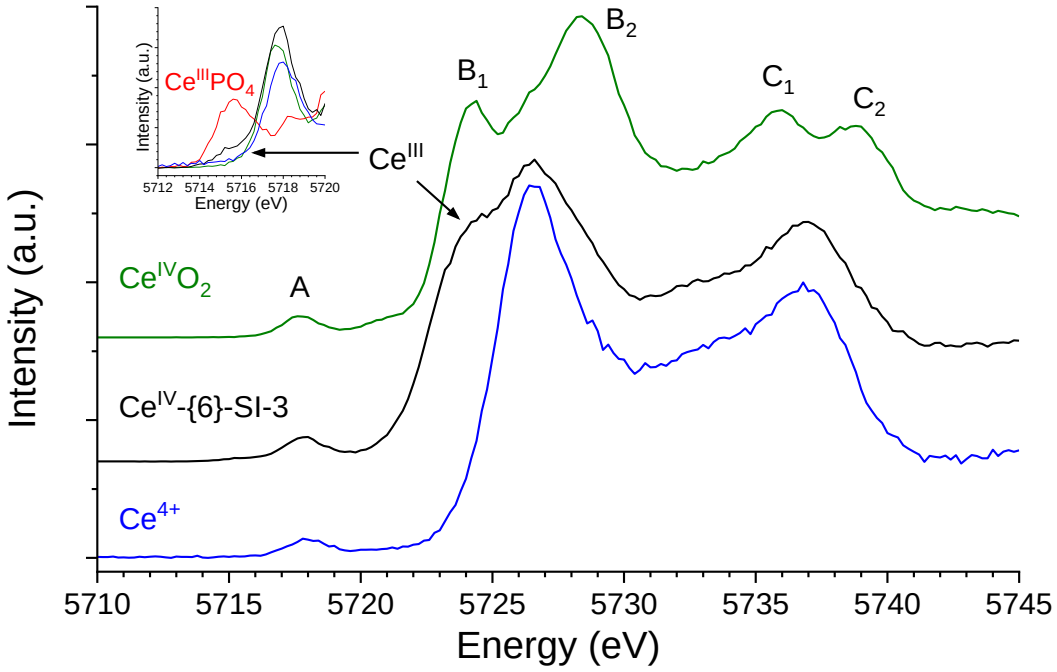

Figure S11. HERFD spectra at Ce L_{III} edge for the Ce-{6}-SI-3 clusters compared to aqueous Ce^{4+} and bulk CeO_2 references. The magnification of the pre-edge was reported in the inserts and compared to monazite as Ce(III) oxidation state reference.

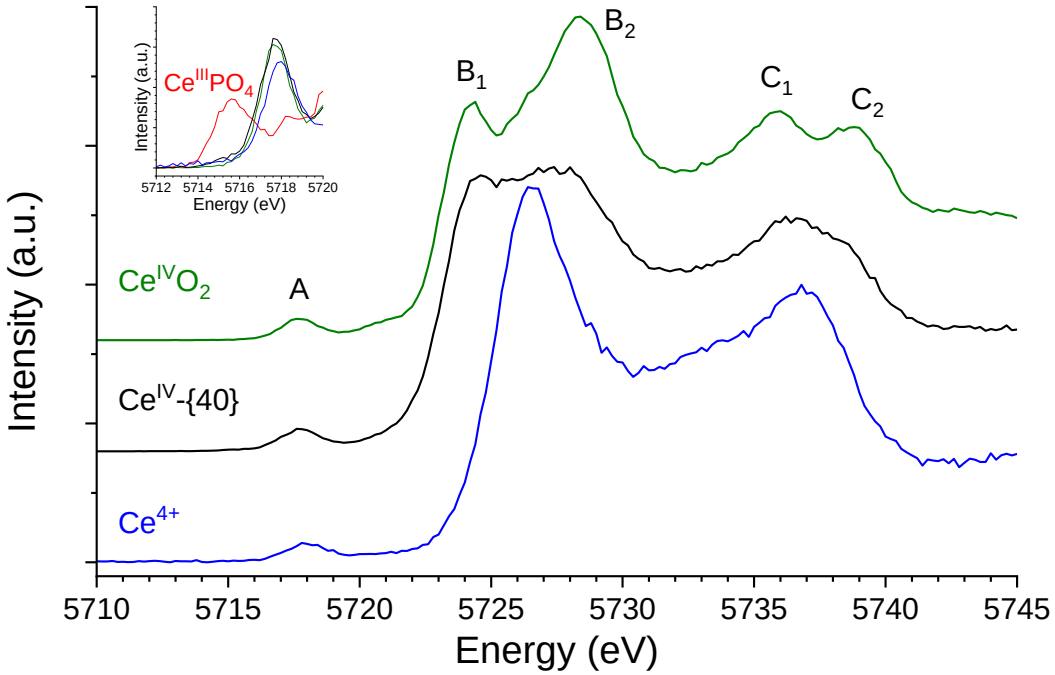

Figure S12. HERFD spectra at Ce L_{III} edge for the Ce-{40} clusters compared to aqueous Ce^{4+} and bulk CeO_2 references. The magnification of the pre-edge was reported in the inserts and compared to monazite as Ce(III) oxidation state reference.

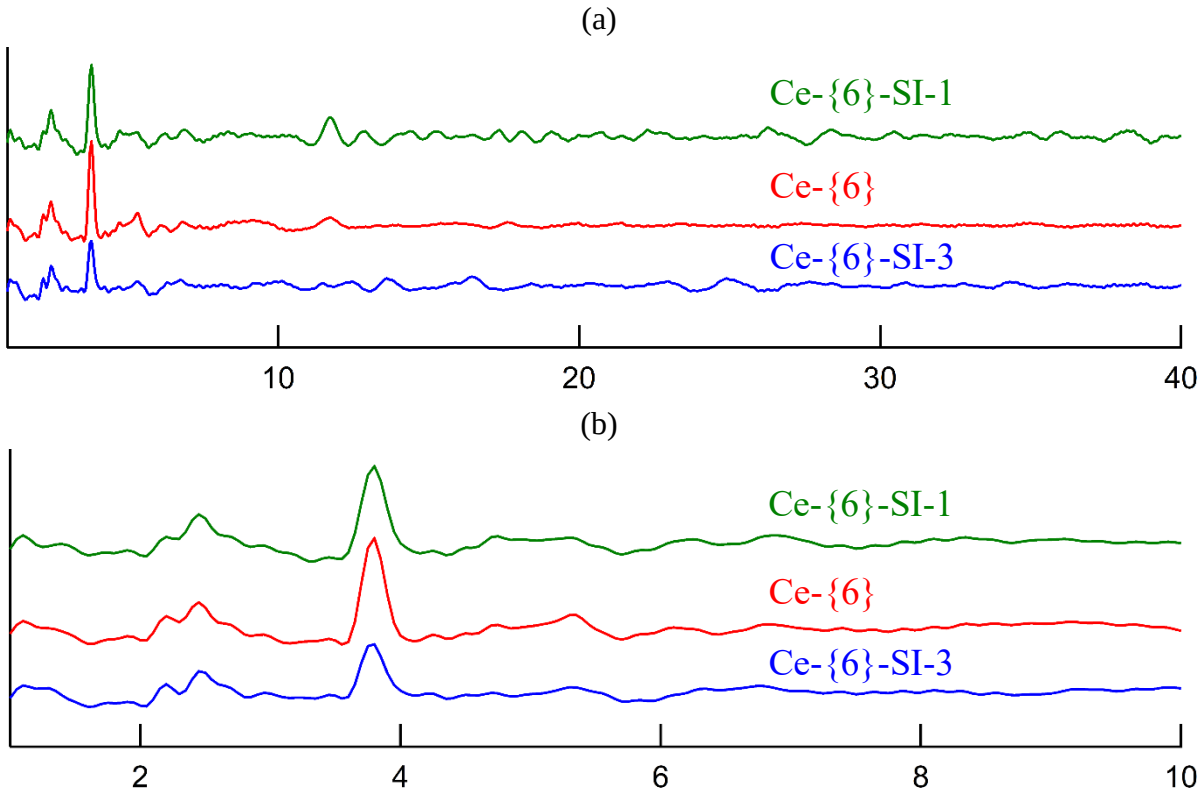

Figure S13. Unscaled PDFs for the Ce-{6}-SI-1, Ce-{6} and Ce-{6}-SI-3 clusters samples in the 1–40 Å (a) and 1–10 Å range (b).

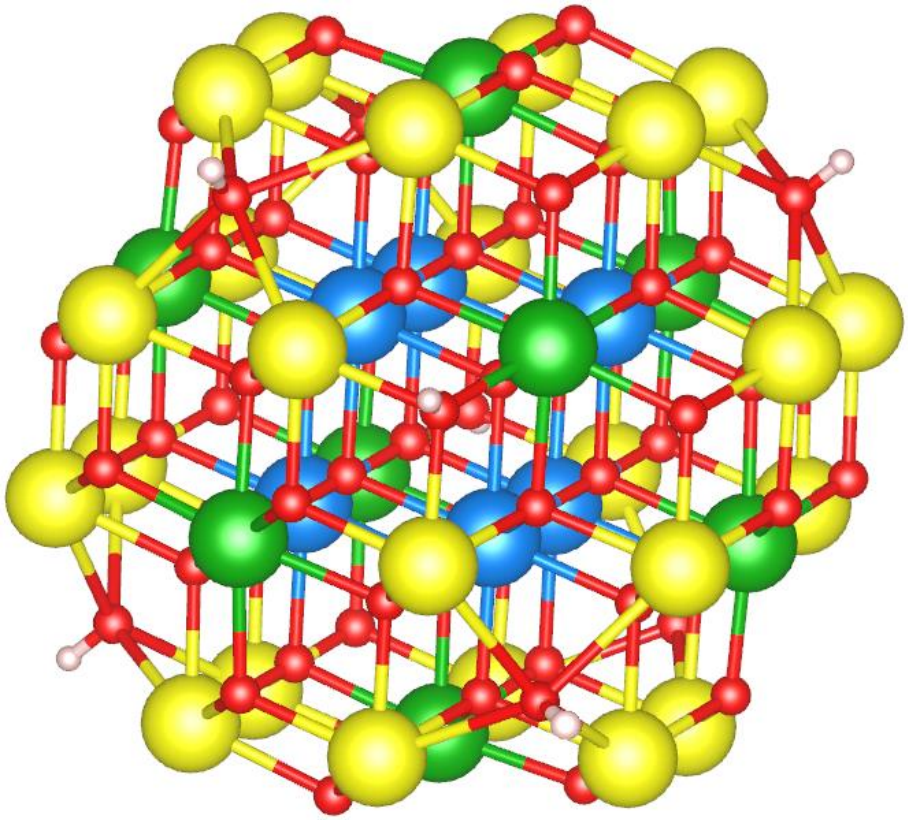

Figure S14. Ce-{38} cluster core representation with the oxygen atoms in red, the hydrogen atoms in white and the cerium atoms in yellow, green and blue. In blue : cerium atoms on the cluster center (seeing 12 cerium atoms in their secondary coordination sphere); in green the intermediate cerium atoms (seeing 9 cerium atoms in their secondary coordination sphere) and in yellow the surface cerium atoms (seeing 7 cerium atoms in their secondary coordination sphere).

Ce-{2} (CN=9)

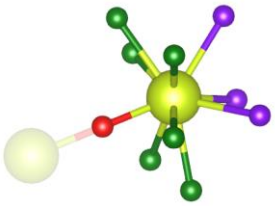

Ce-{6} (CN=9)

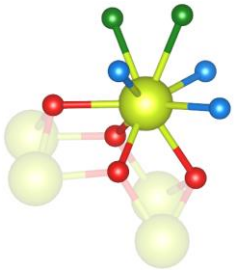

Ce-{38}

Surface (CN=9)	Intermediate (CN=8)	Center (CN=8)
24/38 atoms	8/38 atoms	6/38 atoms

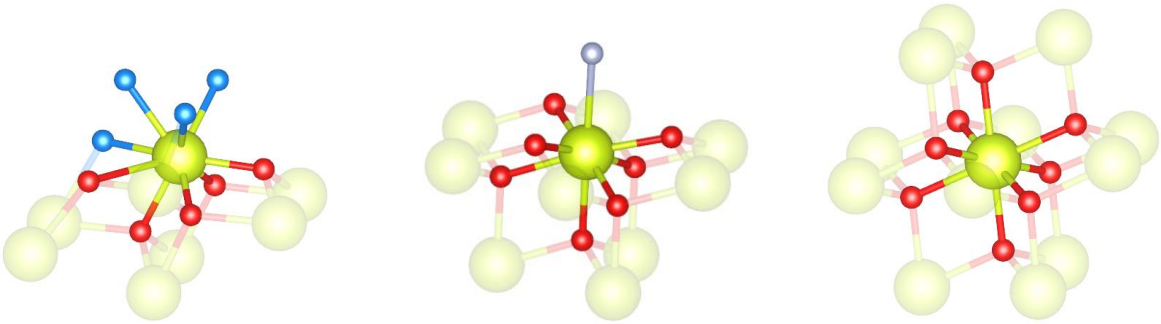

CeO_2 (CN=8)

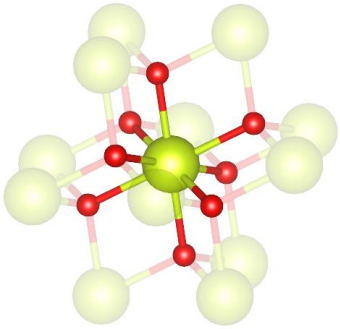

Figure S15. Representation of the cerium atoms first coordination sphere for Ce-{2}, [45] Ce-{6}, [54] Ce-{38} [42] and CeO_2 [38] with the Ce atoms in yellow-green, N atoms in grey, μ-O and μ-OH groups in red, O_{water} in purple, $O_{carboxylate}$ in blue and $O_{nitrate}$ in green. Ce atoms in secondary coordination sphere were shown as shadow.

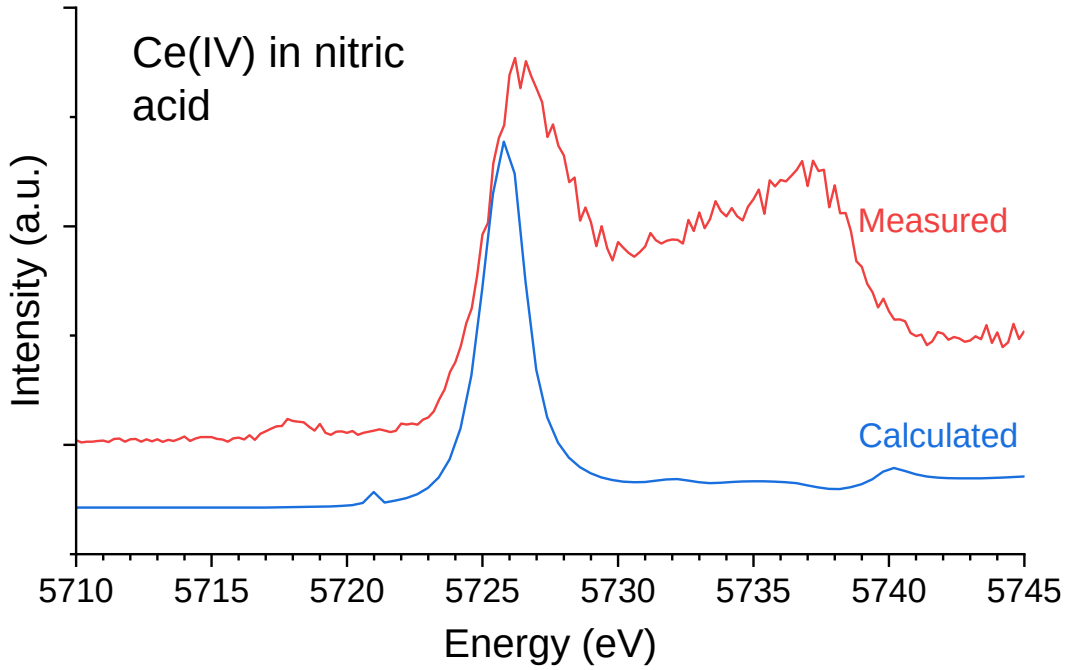

Figure S16. Experimental and calculated HERFD spectra for Ce(IV) in nitric acid media.

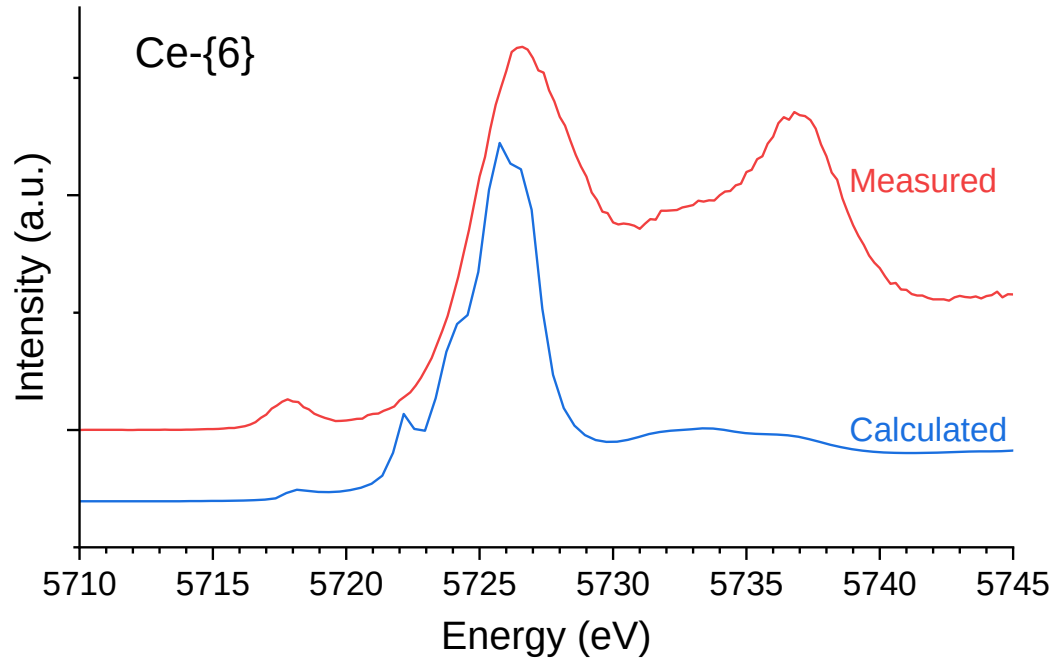

Figure S17. Experimental and calculated HERFD spectra for Ce-{6} cluster.

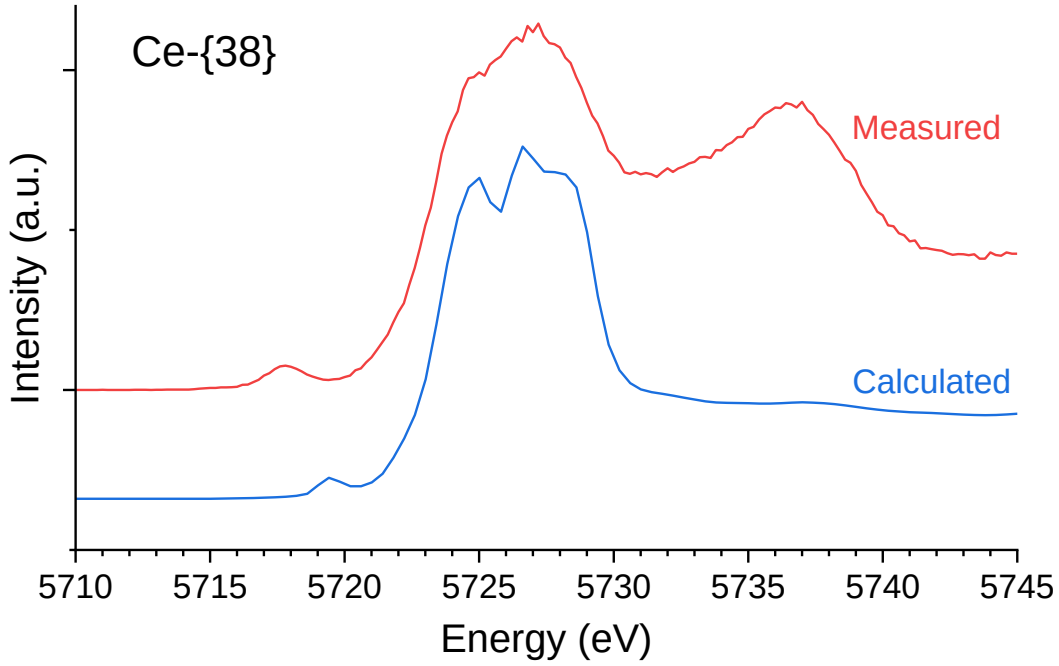

Figure S18. Experimental and calculated HERFD spectra for Ce-{38} cluster.

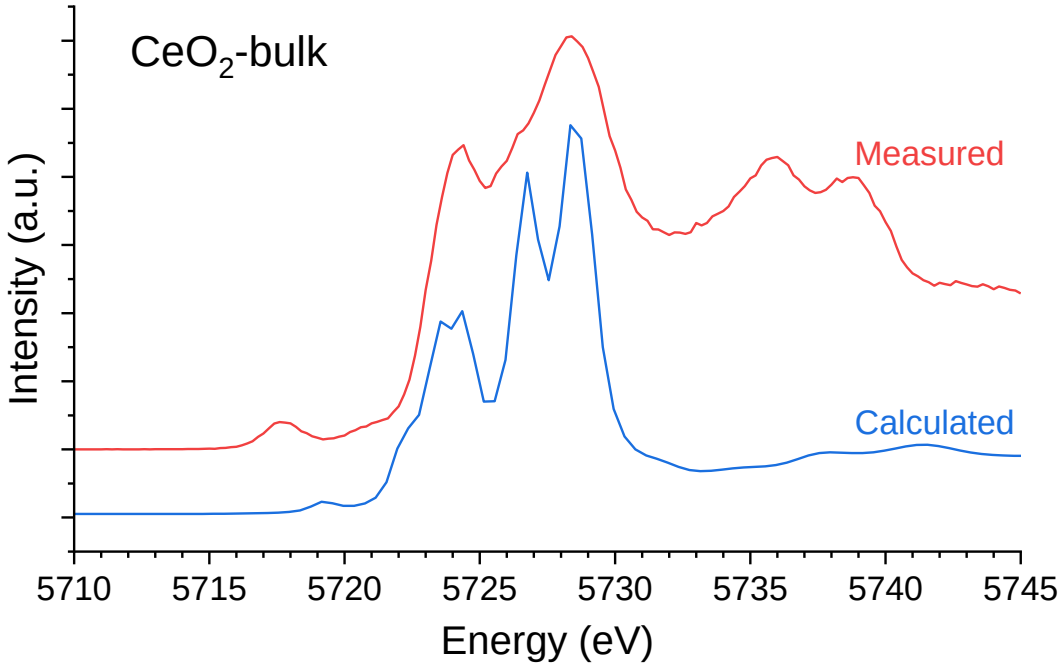

Figure S19. Experimental and calculated HERFD spectra for bulk CeO_2.

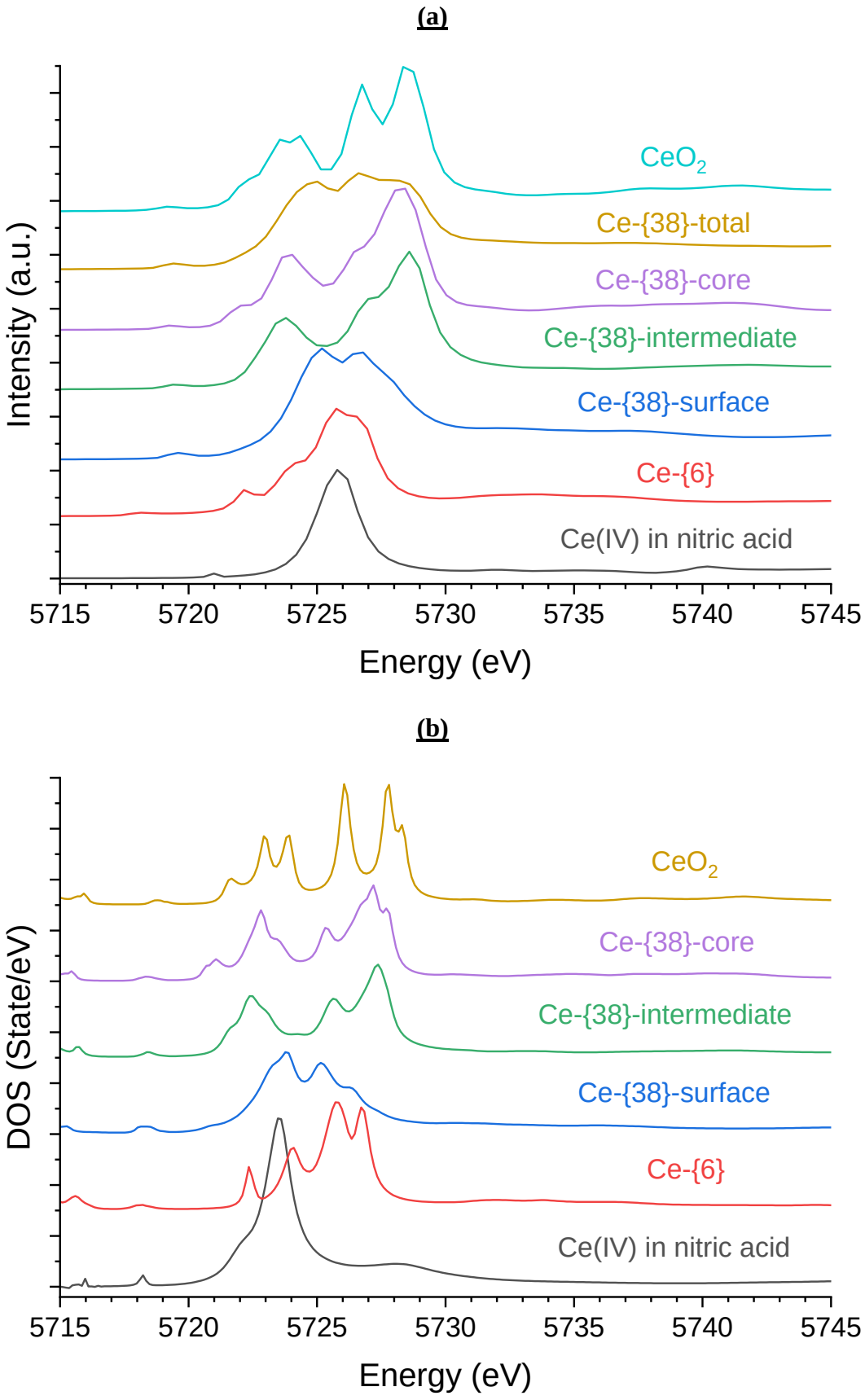

Figure S20. Calculated HERFD spectra and corresponding 5d density of states for Ce(IV) in nitric acid, Ce-{6}, Ce-{38} and bulk CeO_2.

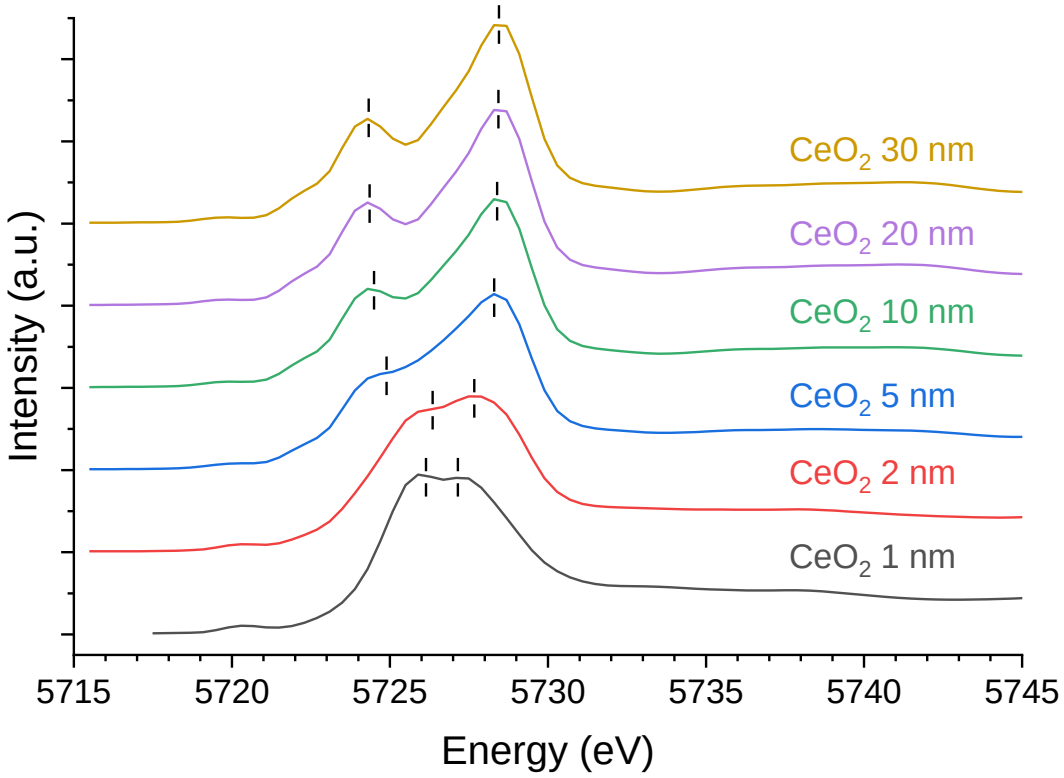

Figure S21. Calculated HERFD spectra for CeO_2 NPs with size ranged from 1 nm to 30 nm.

References

[1] S. L. Estes, M. R. Antonio and L. Soderholm, *Journal of Physical Chemistry C*, 2016, **120**, 5810-5818.

[2] C. Hennig, A. Ikeda-Ohno, W. Kraus, S. Weiss, P. Pattison, H. Emerich, P. M. Abdala and A. C. Scheinost, *Inorganic Chemistry*, 2013, **52**, 11734-11743.

[3] K. J. Mitchell, K. A. Abboud and G. Christou, *Nature Communications*, 2017, **8**, 1445.

[4] I. D. Brown, D. Altermatt, *Acta Crystallographica B*, 1985, **B41**, 244-247.

[5] O. C. Gagné, F. C. Hawthorne, *Acta Crystallographica B*, 2015, **71**, 562-578.

[6] A. Trzeowska, R. Kruszynski, T. J. Bartczak, *Acta Crystallographica B*, 2006, **62**, 745-753.

FOR TABLE OF CONTENTS ONLY

The surface to core properties of cerium oxide nanoparticles are decifered from spectroscopy and simulation performed on set of ceriuum oxo hydroxo clusters of growing size.